Naval Research Laboratory

Washington, DC 20375-5320

Portable Neutron Source
Annual Report

J. Davis
G.M. Petrov

Radiation Hydrodynamics Branch
Plasma Physics Division

May 30, 2008

REPORT DOCUMENTATION PAGE

1. REPORT DATE *(DD-MM-YYYY)* 30-05-2008	2. REPORT TYPE Memorandum Report	3. DATES COVERED *(From - To)* 1 May 2007 – 30 April 2008

4. TITLE AND SUBTITLE

Portable Neutron Source
Annual Report

5a. CONTRACT NUMBER

5b. GRANT NUMBER

5c. PROGRAM ELEMENT NUMBER

6. AUTHOR(S)

J. Davis and G.M. Petrov

5d. PROJECT NUMBER

5e. TASK NUMBER

5f. WORK UNIT NUMBER

7. PERFORMING ORGANIZATION NAME(S) AND ADDRESS(ES)

Naval Research Laboratory
4555 Overlook Avenue, SW
Washington, DC 20375-5320

8. PERFORMING ORGANIZATION REPORT NUMBER

NRL/MR/6720--08-9123

9. SPONSORING / MONITORING AGENCY NAME(S) AND ADDRESS(ES)

Defense Threat Reduction Agency
8725 John J. Kingman Road MS6201
Ft. Belvoir, VA 22060

10. SPONSOR / MONITOR'S ACRONYM(S)

DTRA

11. SPONSOR / MONITOR'S REPORT NUMBER(S)

12. DISTRIBUTION / AVAILABILITY STATEMENT

Approved for public release; distribution is unlimited.

13. SUPPLEMENTARY NOTES

This research was sponsored by the Defense Threat Reduction Agency under Job Order Title "Portable Neutron Source," MIPR No. 07-2193M.

14. ABSTRACT

The angular distribution of neutrons formed in nuclear fusion reactions of a high-energy deuteron beam with a deuterated polyethylene (CD2) was investigated with a Monte Carlo ion beam-target deposition model. The initial conditions were obtained from a two-dimensional particle-in-cell laser-target deposition model. The neutron yield and its angular distribution were studied as a function of peak laser intensity, laser pulse duration and primary target thickness. The proposed scheme for neutron production delivers a typical neutron yield of 10E+5–10E+7 neutrons/ion and 10E+5–10E+7 neutrons/Joule laser energy.

15. SUBJECT TERMS

Neutrons	Target normal surface acceleration	Monte Carlo
Deuterons	Nuclear reactions	

16. SECURITY CLASSIFICATION OF:			17. LIMITATION OF ABSTRACT	18. NUMBER OF PAGES	19a. NAME OF RESPONSIBLE PERSON J. Davis
a. REPORT Unclassified	**b. ABSTRACT** Unclassified	**c. THIS PAGE** Unclassified	UL	50	**19b. TELEPHONE NUMBER** *(include area code)* (202) 767-3278

CONTENTS

Portable Neutron Source

A. Modeling and simulation tools:

1. Laser-target deposition model.

A two-dimensional fully relativistic electromagnetic particle-in-cell model (Ref. [1]) was developed. The particle-in-cell model describes the evolution of the target by moving "quasi-particles" representing each species (electrons and ions). The "quasi-particles" are driven by the laser electromagnetic field. To describe the latter, we solve the Maxwell's equations for propagation of electromagnetic wave (in the visible/near IR) through the plasma. The particle-in-cell model solves the relativistic equations of motion of the charged particles (ions and electrons) from which one can derive detailed information about the particle positions, velocity and energy. Coupling the two parts of the model turned out to be a major problem since the plasma density is very high. Particle-in-cell codes tend to produce "noisy" quantities, such as particle densities and currents. The numerical noise quickly amplifies and the solution is overwhelmed by artificial noise. Therefore, we developed a technique specifically designed to couple a particle-in-cell code to a Maxwell solver. We tested the technique for both underdense and overdense plasma and for laser intensities in the entire range of interest ($10^{16} - 10^{21}$ W/cm^2). The tests we performed were completely satisfactory in terms of accuracy and robustness and indicate that the technique we developed is suitable to describe high-intensity laser-plasma interactions and the production of high-energy ion beams for nuclear fusion and neutron production (Ref. [2]).

2. Ion beam-target deposition model.

A Monte-Carlo code to calculate the angular distribution of neutrons generated by a beam of deuterons was developed. The nuclear fusion reaction considered is $D + D \rightarrow n + {}^3He$ and the target is deuterated polyethylene (CD$_2$), which is widely used in this kind of experiments. The Monte-Carlo code takes into account the actual trajectory of the ion. Ions are launched with prescribed initial energy and direction relative to the target. The ion loses energy, which is accounted for by the energy loss function. The stopping power is calculated from the stopping powers of deuterons in carbon and deuterons in deuterium. The (high-energy) deuterons are also scattered due to collisions with the target material; therefore their trajectories are not a straight line. The ion energy and trajectory are followed in time and space until the ion energy becomes less than a prescribed cut-off energy (~1 KeV). During each time step the neutron flux to specific directions of observations is also calculated from the differential cross section. The model outputs the angular distribution of neutrons, as well as the total neutron yield.

3. Coupling of the laser-target and ion beam-target deposition models.

The two models can, in general, be used independently. Here they are connected since the output of the *laser-target deposition model* (deuteron velocity and energy) serves as input of the *ion beam-target deposition model*. The laser-target deposition model outputs the energy and direction of every deuteron tracked in the simulations, which is precisely the input for the Monte-Carlo code. The output of the Monte-Carlo code is the angular distribution of neutrons and the total neutron yield (in absolute units).

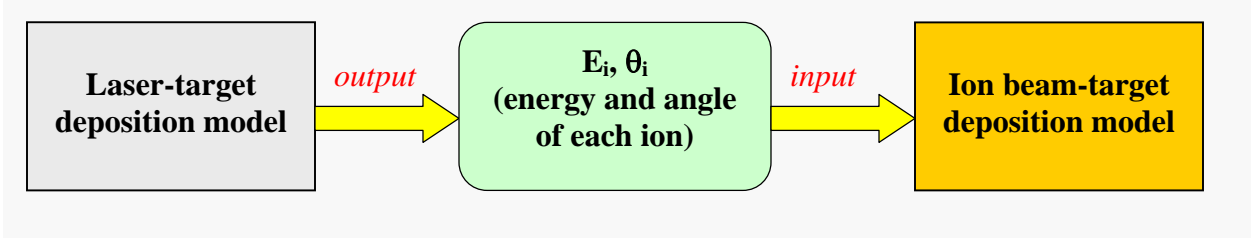| Laser-target deposition model | *output* → | E_i, θ_i (energy and angle of each ion) | *input* → | Ion beam-target deposition model |

Fig. 1 Coupling of the laser-target deposition model (the electromagnetic particle-in-cell model) to the Monte Carlo ion beam target deposition model.

B Sample results and accomplishments:

1. Double-layer target

The formation of a high-energy deuteron beam from the interaction of ultra-short laser pulses with a planar double-layer solid target was investigated. The target is a two-layer thin foil with thickness of ~1 μm. The front layer, which accounts for most of the target mass, is made of high Z material. We chose gold, which is commonly used. The rear layer is very thin ($0.02 - 0.1$ μm) and it is made of deuterium-containing material (for simplicity we assumed that it is made of pure deuterium). Using the particle-in-cell model, we studied a range of parameters for which a highly directional deuteron beam is created. We varied the following laser-target parameters: (a) peak laser intensity: from 10^{18} to 10^{21} W/cm^2, (b) laser pulse duration: from 40 to 160 fs, and (c) target thickness: from 0.1 and 3 μm. The goal is to establish trends and scaling laws, as well as a suitable range of (laser and target) parameters that can be met in experiments. Figure 2 summarizes two important quantities related to laser energy deposition: mean energy of the ion beam and conversion efficiency of laser energy to ion energy. The regions for which MeV ions are generated are shown in green. Figure 3 plots the ion beam energy and angular distribution vs. target thickness. One can see, for example, that thinner targets produce more energetic ions (Fig. 3a, top left). Intermediate thickness favors ion beam directionality (Fig. 3d). Large target thickness (> 1 μm) leads to both poor directionality (Fig. 3h) and low energy (Fig. 3g) of the ion beam.
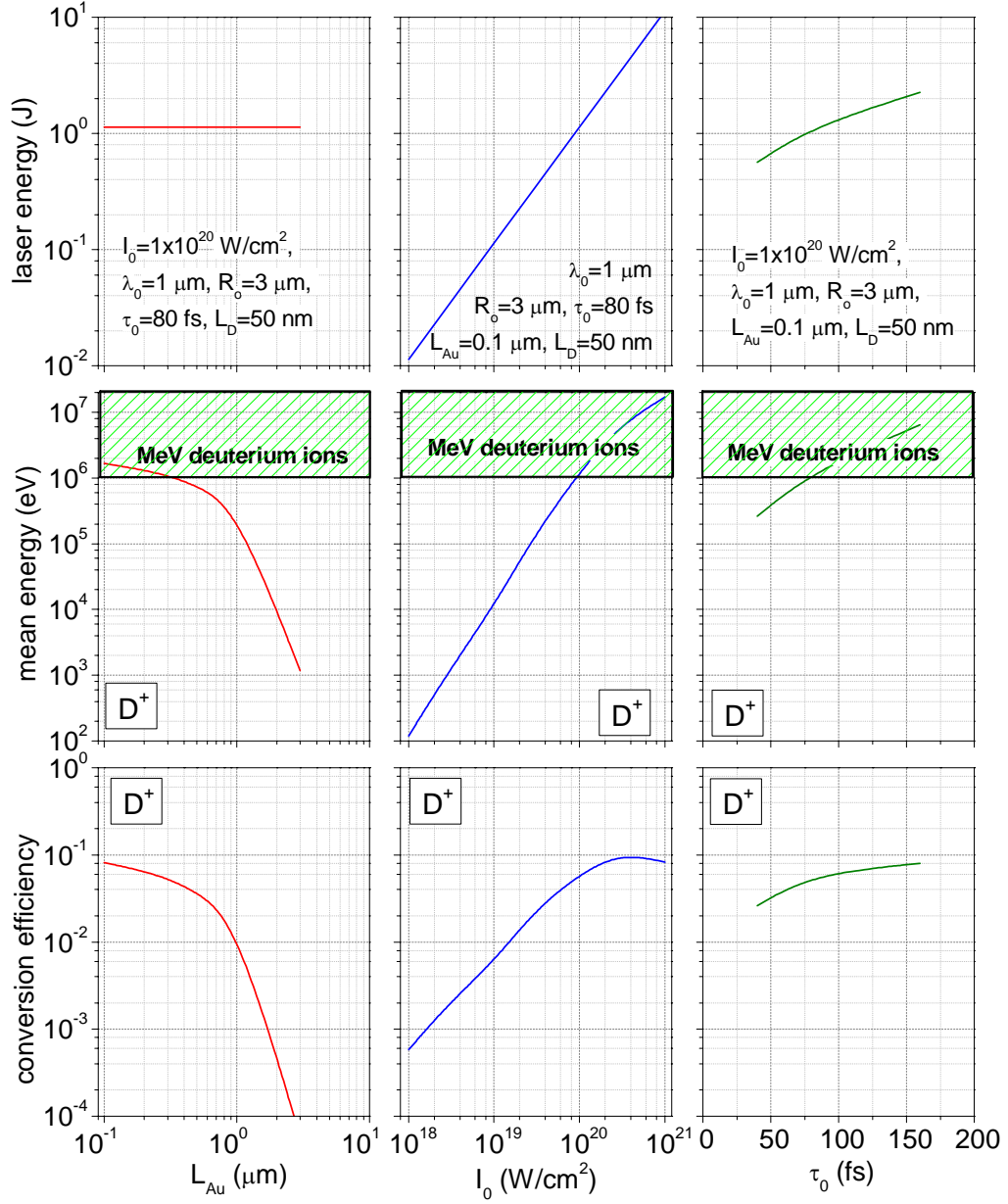
Fig. 2. Laser energy (top row), mean energy of D^+ (second row); and energy conversion efficiency of D^+ (bottom row) as a function of target thickness (left column), peak laser intensity (center column) and laser pulse duration (right column).
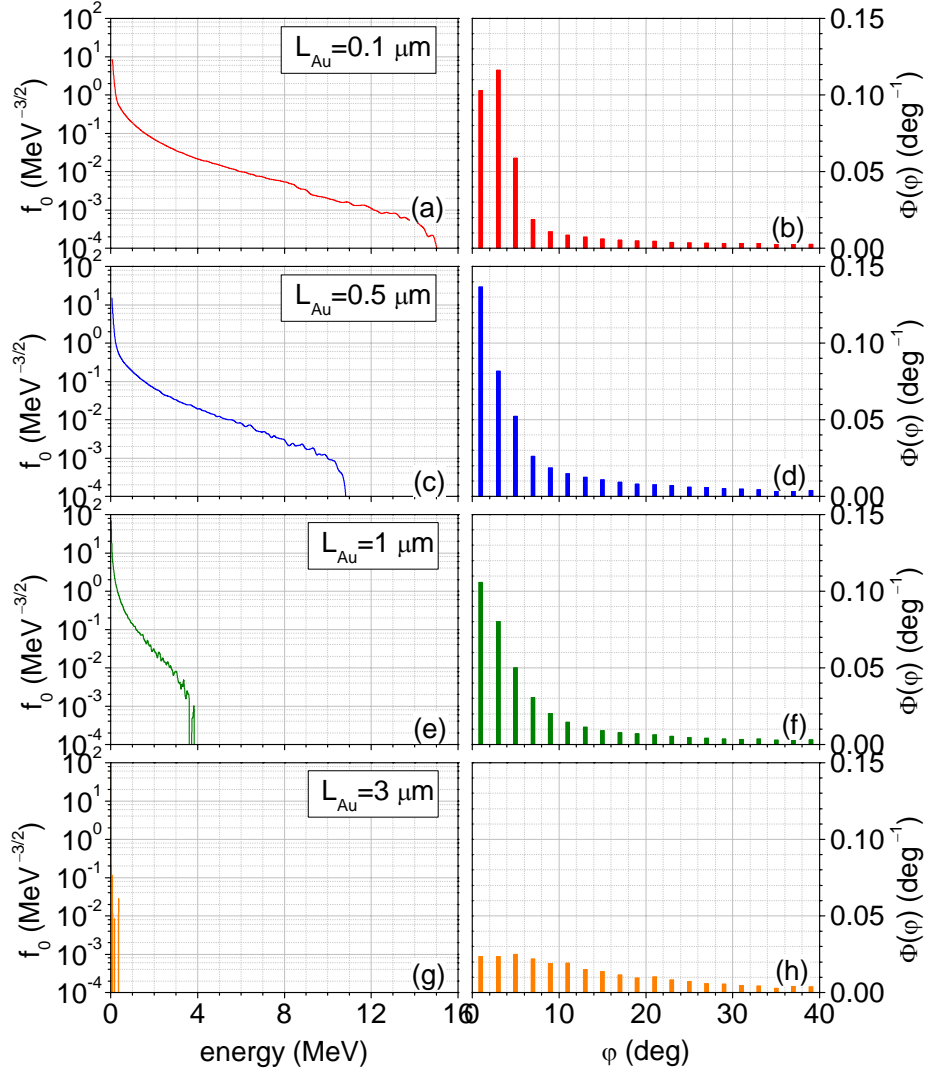
Fig. 3 Deuteron energy distribution function (left column) and angular distribution function (right column) for different target thicknesses. All parameters are as in Fig. 2.

The next step is to calculate the neutron yield from the ion beam-target deposition model. The secondary target is a thick (~ 1mm) slab of deuterated material (CD_2). The Monte-Carlo model follows the deuteron trajectories in the target and calculates simultaneously the neutron flux to specific directions of observations. Figure 4 displays a typical angular distribution function of neutrons from a CD_2 target. In Fig. 4 we plot the number of neutrons per unit angle: per steradian (left) and per radian (right). A substantial number of neutrons are emitted at small angle ($0–20^0$). The total number of neutrons is 2×10^6 at laser energy of 1.1 J.

4
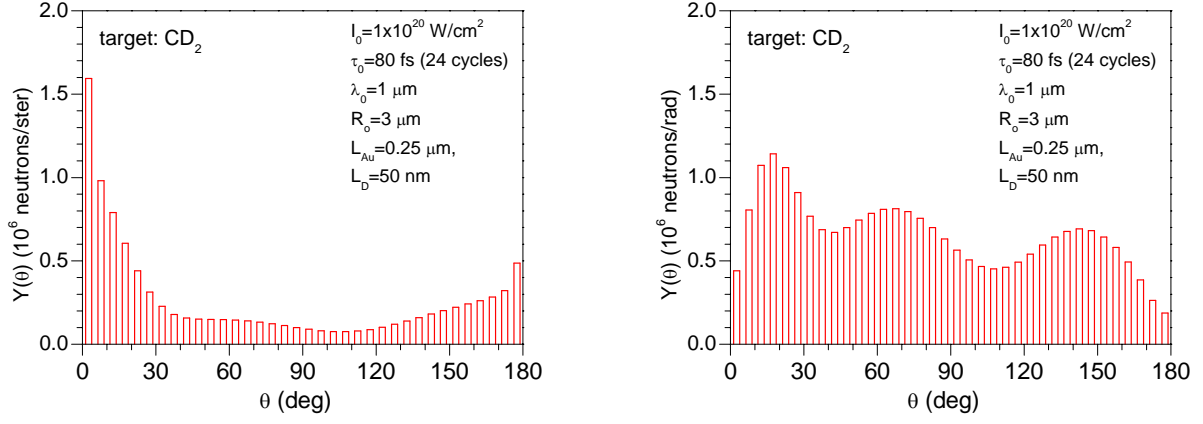
Fig. 4 Angular distribution function of neutrons per steradian (left) and per radian (right).

Figure 5 (below) summarizes our parametric study.
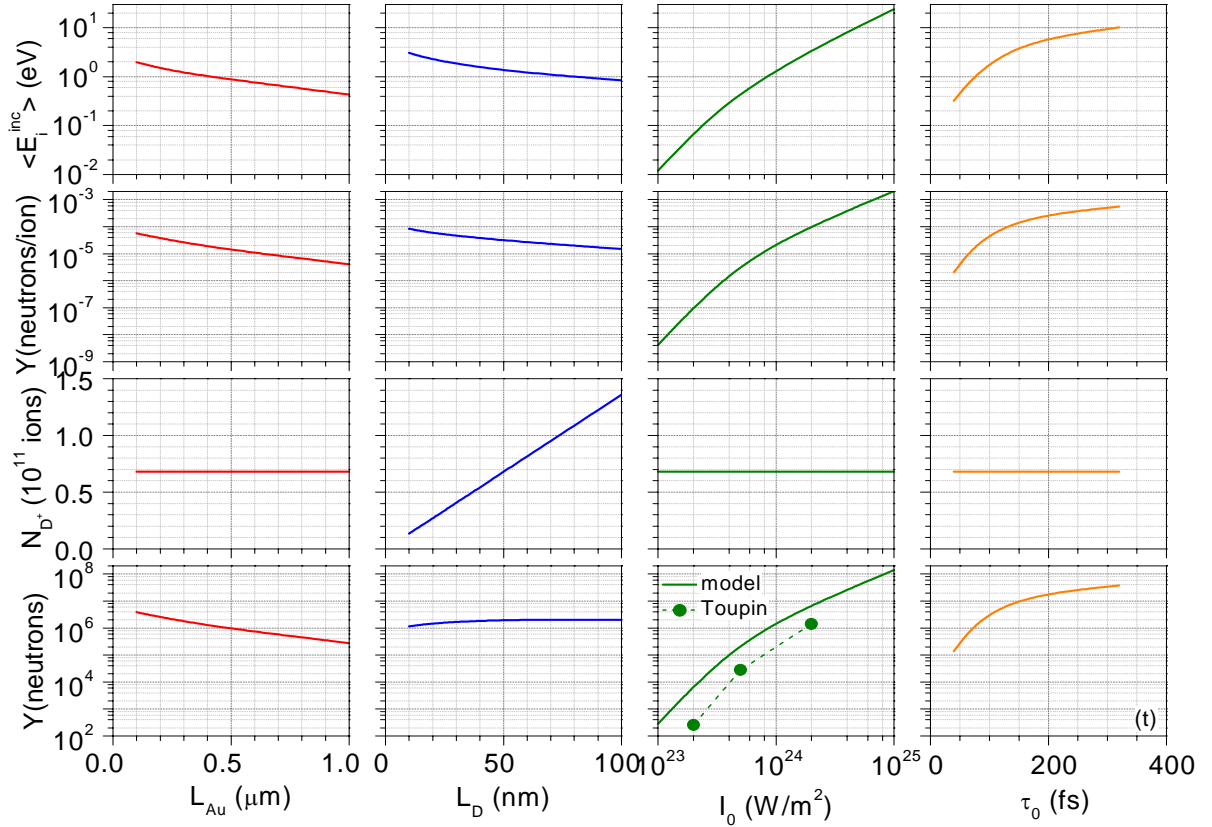
Fig. 5 Average deuteron energy (first row); neutron yield per ion (second row), total number of deuterons (third row) and total neutron yield (last row) for different *Au* layer thickness (first column), *D* layer thickness (second column), peak laser intensity (third column) and laser pulse duration (right column). Symbols – simulations by Toupin *et al* (Toupin C, Lefebvre E, and Bonnaud G 2001 *Phys. Plasmas* **8** 1011).

Figure 5 plots the average incident deuteron energy $<E_i^{inc}>$, the total neutron yield per ion, the number of deuteron ions and the total neutron yield are plotted vs. thickness of the gold and deuterium layers, peak laser intensity and laser pulse duration. For the intermediate peak laser intensity of $I_0 = 10^{24} \ W/m^2$ the neutron yield is $10^5 - 10^7$ neutrons, depending on the laser pulse duration. The results shown so far have been analyzed in detail and are published in Plasma Phys. Control. Fusion (Refs. [3]).

2.Uniform target

The target design of the double-layer target offers a lot of flexibility; in particular, it allows us to control the deuteron energy and angular distribution. It has, however, a few drawbacks. Complications may arise due to alignment of the two targets, etc. Another problem is the disparity of thicknesses of the primary and secondary targets (primary target for ion acceleration, secondary target for neutron generation). The secondary target must be thick, of the order of ~1 mm, in order to be able to stop all energetic (~MeV) deuterons, while the primary target is very thin (~1 μm), making it fragile and susceptible to damage and mis-alignment. A remedy to these problems is to use a thicker uniform target, which can be made of the same material as the secondary target. This approach allows consolidation of the primary and secondary targets to form a single target. The key issue, target robustness, is now achieved by the target thickness (~1 mm). This is, perhaps, the main reason such targets, made either from CD_2 or CD, are employed in virtually all experiments. The objectives are to study the ion generation, and consequently, the neutron generation from a single-layer CD_2 target and to compare it with the neutron generation from its counterpart, a double-layer target. This will help us design better targets for more efficient neutron generation.

Extensive simulations with the new target: a planar uniform CD_2 target was carried out. Two aspects of the neutron production from high-intensity ultrashort pulse lasers prompted the present study: (i) the controversies related to target design (material, dimensions, etc.); and (ii) studying realistic targets employed in actual experiments. We address the first issue by comparing two targets: a "thick" ($>> 1$ μm) uniform piece of deuterated plastic (CD_2) and a double-layer "thin" (≤ 1 μm) foil. The second issue is addressed by comparing simulation results with experimental data. First, we studied the deuteron acceleration mechanism from a planar uniform CD_2 target. It originates from the rear target surface via Target Normal Sheath Acceleration with a modest contribution from the bulk of the target.

Figure 6 displays typical energy and angular distribution functions from a uniform and double-layered target for equal laser parameters. The double-layered target produces more energetic ions (a) and strongly forward-peaked angular distribution (c). The ion energy and angular distributions appear to be very different compared to the previous, double layer target.
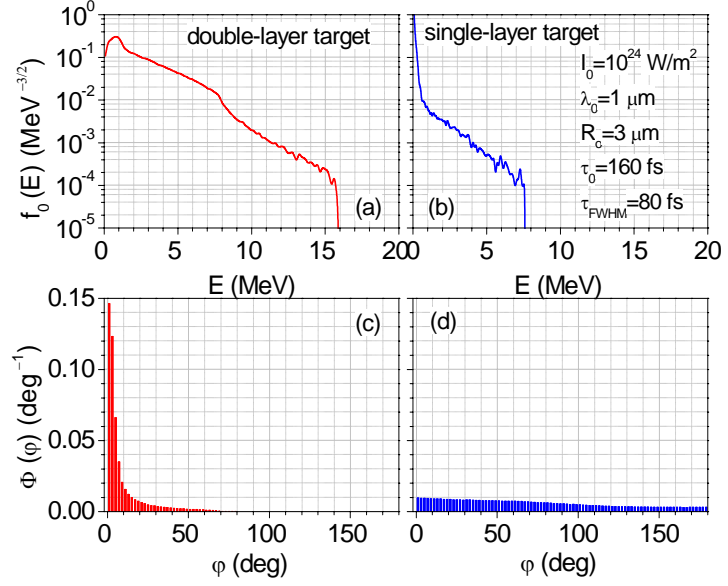
Fig. 6 Energy (a) and (b) and angular (c) and (d) distribution function of deuterons from a double layer (Au+D) target (left) and single layer (CD_2) target (right).

However, we found that in both cases about the same amount of energetic (above 1 MeV) deuterons are produced, of the order of 10^{10}–10^{11}. The deuterons from the double-layer target (blue triangles) are somewhat more energetic compared to the uniform target (red open squares). Figure 7 plots the maximum deuteron energy from a uniform and double-layer targets.
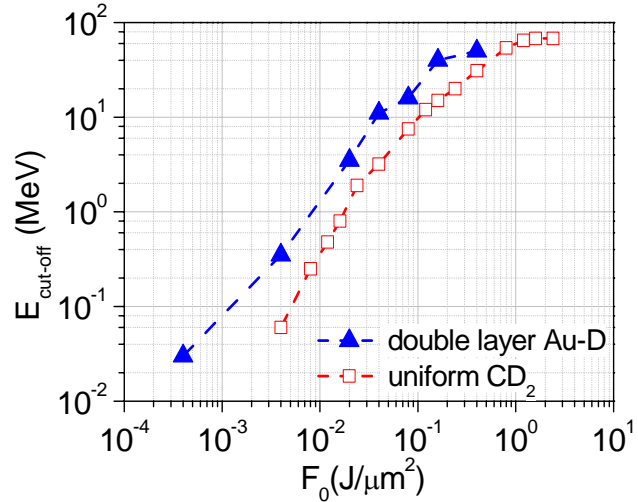
Fig. 7 Maximum deuteron energy vs. laser fluence for double-layer and uniform targets.

The main difference between the two is the deuteron angular distribution: thin (sub-micron) double-layer targets produce a core of high-energy collimated (10–20°) beam of deuterons, while "thick" (several micron) uniform targets produce a high-divergence beam of deuterons with somewhat lower energies.

Next, we investigated the neutron yield in absolute units. The double-layer target is more efficient, but with the laser energy increasing the differences between the two targets diminish. Above about 10 J both give comparable neutron yields.

Comparing model predictions of the neutron yield with experimental data benchmarked the simulation. The model predictions are in good agreement with measured neutron yields over a wide range of laser energies, spanning two orders of magnitude.
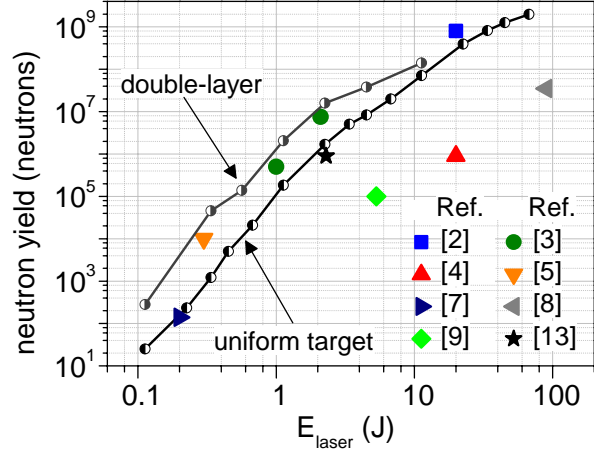

Fig. 8 Neutron yield from a uniform CD_2 target and double layer target vs. laser energy. Solid line with symbols – model predictions for double-layer and uniform targets; symbols – experiments.

Influence of the preplasma

3. Target design

We continue our investigations focusing on the target design. We studied double-layer vs. uniform targets and simultaneously "thick" ($\gg 1$ μm) vs. "thin" (≤ 1 μm) targets. We established that double-layer targets tend to perform better, especially in terms of angular distribution of deuterons and neutrons. All previous studies have been limited to planar targets (Fig. 1 top), which are the simplest and most straightforward. Shaping targets is known to improve the ion beam quality, making it, for example, more laminar or mono-energetic. Therefore our next goal is to perform simulations with more complex (in terms of shape) targets.

We will first study the impact of the pre-plasma on the neutron production. The pre-plasma occurs during the interaction of a planar target with the foot of the laser pulse. This laser pre-pulse is always present and may change the target geometry by ionizing the irradiated front surface of the target. A layer of plasma is formed, called pre-plasma, the extent of which depends upon the parameters of the laser pre-pulse. Figure 1 top shows an "ideal" planar target, unaffected by the laser pre-pulse. Figure 1 bottom shows the more realistic situation of a planar target with a pre-plasma. The pre-plasma length can be (at least conceptually)
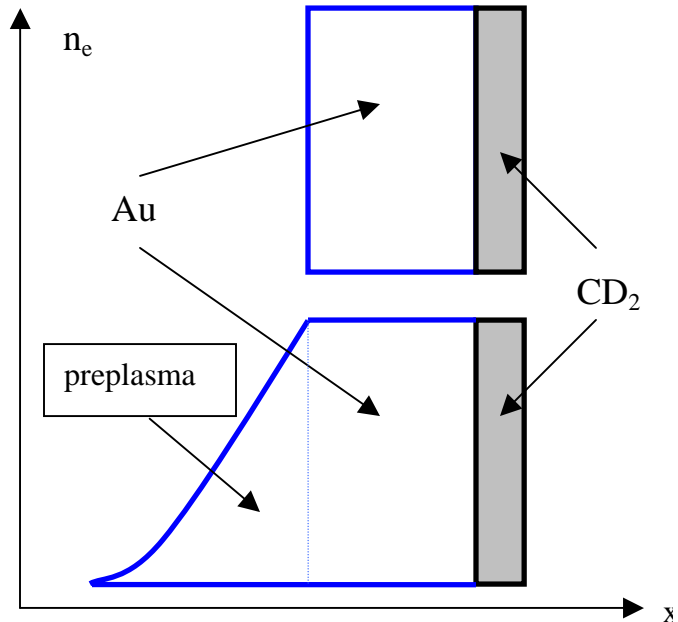
controlled to some degree by varying the intensity of the laser pre-pulse.

Fig. 1 Planar target (top) and a target with a pre-plasma (bottom). The thickness of the CD_2 layer is 50 nm.

The neutron yield in absolute units vs. pre-plasma length is shown in Fig. 2 for three thicknesses of the Au layer. The points to the left at 0.02 μm mimic "ideal" planar target. As it can be seen there is an optimum pre-plasma thickness of the order of 0.1–0.3 μm, for which the neutron yield peaks. So the presence of some pre-plasma is actually helpful for the neutron production.

The thicker the target, the more pronounced is the pre-plasma impact (green line & triangles, corresponding to Au layer of 1μm). The neutron yield can increase by a factor of ~100 compared to "ideal" targets with no pre-plasma. In any case the pre-plasma (and the target shape in general) appears to be important for the neutron production.
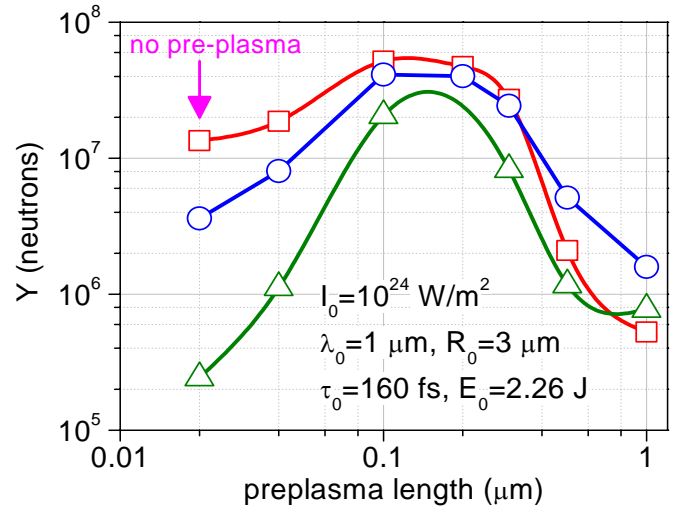

Fig. 2 Neutron yields from a double-layer Au-CD_2 target vs. pre-plasma length. The three curves are for a thickness of the Au layer of 0.25 μm (red square), 0.50 μm (blue cycles), and 1 μm (green triangles).

APPENDIX

REPRINTS

Energy and angular distribution of deuterons from high-intensity laser–target interactions

G M Petrov and J Davis

Naval Research Laboratory, Plasma Physics Division, 4555 Overlook Ave SW, Washington, DC 20375, USA

E-mail: george.petrov@nrl.navy.mil and jack.davis@nrl.navy.mil

Abstract

The formation of a high-energy ion beam suitable for driving nuclear fusion reactions and producing MeV neutrons was investigated. The interaction of intense ultra short laser pulses with a double-layer thin foil for the production of MeV deuterons was studied theoretically and numerically simulated using a two-dimensional electromagnetic particle-in-cell model. The directionality and energy of the deuteron beam, specifically the conversion efficiency of laser energy into deuteron kinetic energy, and deuteron energy and angular distribution functions are studied as a function of peak laser intensity, laser pulse duration and target thickness. A range of parameters was determined for which a highly directional deuteron beam is generated.

(Some figures in this article are in colour only in the electronic version)

1. Introduction

High-intensity ultrashort pulse lasers are compact and versatile systems for inducing nuclear fusion reactions. It has been known for some time that when high-intensity laser radiation interacts with solid targets, it creates energetic particles, capable of driving fusion reactions. The remarkable progress in the development of laser-based particle accelerators is pushing the frontiers in basic research and holds promise for harnessing nuclear fusion for practical applications. As laser systems producing ultrashort high-intensity pulses are expected to become more compact and affordable several advanced applications can be envisioned, such as positron emission tomography [1], cancer therapy [2,3] and laser-induced nuclear reactions [4]. Laser-driven neutron sources are an alternative to the accelerator- and reactor-driven sources offering high brightness, compactness, short duration, shielding and relatively low cost. This is particularly advantageous for applications such as fast neutron radiography [5], transmutation of nuclear waste [6] and fusion research [7].
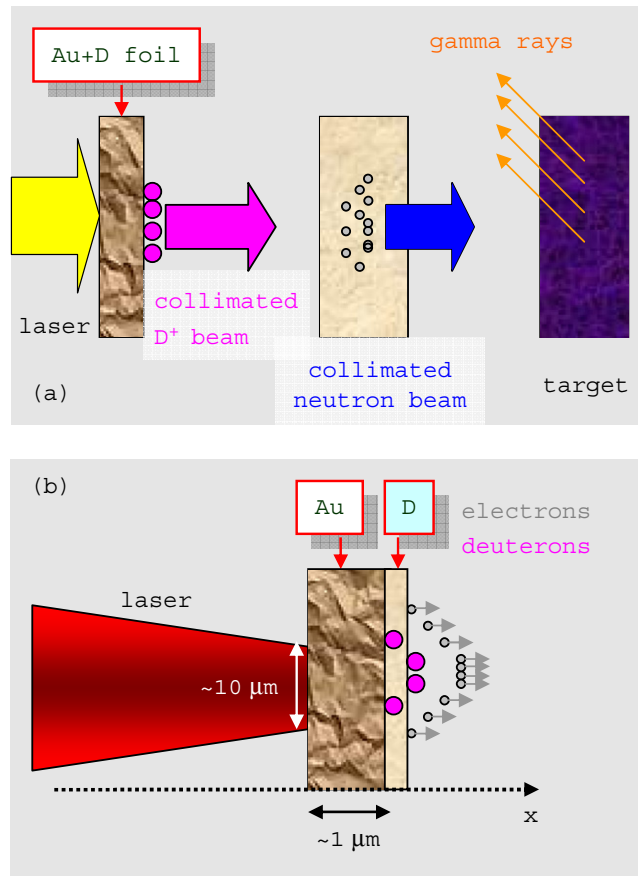
Figure 1. Neutron production concept (*a*) and target configuration (*b*). The laser pulse propagates from left to right along the axis '*x*', the laser electric and magnetic fields are along the '*y*' and '*z*' axes, respectively.

For our purposes neutron production can be visualized schematically as shown in figure 1(*a*). During the first stage, a high-energy ion beam is generated. In the next stage, fast neutrons are born in fusion reactions driven by the fast ions. During the third stage, the neutrons impinge on the target of interest and the interaction of the fast neutrons with the target leads to the emission of gamma rays. The gamma-ray 'signature' is unique for each element and, in principle, can be used to identify the constituents of the material producing them. The real challenge is to produce a neutron beam in sufficient numbers (10^7–10^{10}) that is reasonably well collimated ($10°$–$20°$ divergence). The difficulty is rooted in the precursor, the ion beam, which must be both energetic and highly directional. The ion energy must be comparable or higher than the knock-off neutron energy (typically $\sim$2.5 or $\sim$14 MeV). Only then the neutrons born in nuclear fusion reactions are scattered preferentially in the forward direction. Thus we focus our attention on laser–target interactions capable of producing energetic deuteron beams with small divergence.

Ion acceleration can be achieved by various types of laser–target interactions: underdense plasmas, clusters and solids. Generation of multi-MeV ion beams with narrow angular spread has been demonstrated in the interaction of high-intensity ultrashort pulse lasers with

2

underdense plasma [8, 9]. Neutron production from nuclear fusion reactions in laser–cluster interactions has also been demonstrated [10]. The most attractive feature of this approach is the use of off-the-shelf laser systems as nuclear fusion reactions can be triggered at peak laser intensities as low as $\sim 10^{20}\,\mathrm{W\,m^{-2}}$ ($\sim 10^{16}\,\mathrm{W\,cm^{-2}}$). Unfortunately, the neutrons created by laser–cluster interactions are scattered isotropically [11] and their number is only of the order of 10^4–10^6 per shot [12, 13]. Therefore clusters are not suitable for generation of an energetic focused beam of neutrons. Laser-driven ion acceleration and generation of fast neutrons can also be achieved as a result of ultraintense laser irradiation of solid targets [14, 15]. It is now well established that ions at the rear surface of a thin ($\sim 1\,\mu$m) foil can be accelerated to relativistic energies by the electrostatic field of a space-charge potential created by escaping non-thermal electrons and the ions that are left behind. This mechanism is known as target normal sheath acceleration (TNSA) [15–17]. Recent work by Sentoku *et al* elaborated on this widely accepted mechanism of ion acceleration from the rear surface of the target. They found that the effect of electron recirculation enhances the peak proton energy if the target thickness is shorter than half of the laser pulse length [18]. When the target thickness becomes comparable to the plasma skin depth, the laser penetrates to the rear of the target and TNSA transitions to the so-called 'laser breakout afterburner' regime [19]. This regime distinguishes three stages of ion acceleration: a period of TNSA, followed by a period of enhanced TNSA during which the cold electrons are converted into hot electrons and rapid ion acceleration in the enhanced longitudinal electrostatic field. At intensities exceeding $10^{25}\,\mathrm{W\,m^{-2}}$ laser-induced shocks could also accelerate ions to high energies [20]. At even higher intensities, for which the dimensionless laser field amplitude becomes comparable to the ratio of ion-to-electron mass, direct laser acceleration of protons to relativistic energies becomes possible [21]. Regardless of the acceleration mechanism, if the foil parameters are properly chosen, a well-collimated beam of light ions can be accelerated to energies in the MeV range. Recent progress in ultrashort pulse laser technology now allows generation of laser pulses with intensities which are adequate for producing an ion beam with the required parameters. In spite of the practical challenges of implementing such laser systems, both the ion beam collimation and high energy are crucial for production of high-flux neutron beam.

Neutron generation in high-intensity laser-foil interaction has been demonstrated experimentally [22–31] and theoretically [7, 32–35]. Perkins *et al* [7] surmised various regimes of laser–target interactions depending on target configuration and peak laser intensity. Of particular interest are the results by Toupin *et al* [33], which studied the angular distribution of neutron emission as a function of laser intensity and maximum electron density. Their results indicate that if the medium generating light ions is highly overdense plasma (typical for laser-thin foil interaction), the neutrons are emitted preferentially in the forward direction. Macchi *et al* [35] studied the acceleration of ion bunches by using an analytical model as well as one- and two-dimensional particle-in-cell (PIC) models. They were concerned mostly with the formation of high-density low-energy (<1 MeV) ion beams, which are not optimal for the formation of directional neutron beams. To our knowledge, there is no systematic theoretical study regarding the formation of collimated deuteron beams, except for [33–35]. Our objective is to study theoretically the formation of a collimated beam of high-energy (MeV) deuterium ions as a result of the interaction of high-intensity laser radiation with thin double-layer foil. This is considered as the first stage of a general scheme leading to the generation of directional neutron beams. Our primary interest is in studying the directionality and energy of the deuteron beam, specifically (i) the conversion efficiency of laser energy into ion kinetic energy, (ii) ion energy distribution function and (iii) ion angular distribution function. These data will later serve as input parameters of a model simulating the production and scattering of the neutron beam. In section 2 we outline the target configuration and the approach we use to model the

laser–target interaction. In section 3 we report on results for a specific target and summarize our findings in section 4.

2. Laser–target interaction model

To simulate the interaction between intense laser radiation and solid target we implemented a 2D relativistic electromagnetic PIC method. The target is approximated as a slab of overdense plasma whose constituents (electrons and ions) are modeled with the PIC method. The propagation of laser radiation into the plasma is modeled by solving the Maxwell equations. Other numerical models that adopted this approach have been developed for 2D [35–56] and 3D [21, 57–62] geometry. Our version of a 2D model is given in appendix, where the coupling of the electromagnetic solver to the PIC code is described. Here we will provide only a brief account for the reasons that prompted us to develop this algorithm. The most obvious approach to couple the PIC method to a Maxwell solver is to calculate the current density from PIC, substitute it into the Maxwell equations and solve them for the electromagnetic field. This two-step procedure is repeated for each time step. This intuitive approach, however, suffers from some deficiencies. PIC codes are notorious for producing 'noisy' quantities, such as particle densities and currents. The numerical noise quickly amplifies and spurious numerical solutions are generated. Therefore strategies that exploit the specific nature of the PIC method must be sought to remedy the problem of numerical instability. We implemented a relationship between the laser electric field $\vec{E}$ and current density $\vec{j}$ generated by the movement of charged particles for the special case when $\vec{j}$ is calculated from a 2D PIC model in Cartesian coordinates:

$$\vec{j}^{n+1/2} = \hat{\sigma}^{n+1/2}\vec{E}^{n+1/2} + \Delta\vec{j}^n. \tag{1}$$

Equation (1) is concisely written in matrix form, in which $\hat{\sigma}$ is a 2×2 matrix with elements calculated from quantities such as particle mass, charge, density, relativistic factor and cyclotron frequency (appendix). The superscript denotes the discretization time level with 'n' being the previous and $n + 1$—the new time level. If the current density (1) with the *electric field factored out* is substituted into the Maxwell equations, the numerical scheme becomes very robust. Numerical noise and grid heating are strongly suppressed and spurious numerical solutions are eliminated. The technique is applicable to modeling the interaction of laser radiation with both underdense and overdense plasmas, but it is particularly useful for highly overdense plasma ($\sim$100 times the critical electron density), where other techniques have difficulties or fail. Decomposition of the current density in the form (1) has also been used in other electromagnetic PIC models, but the specific numerical implementation may have been different from ours [63, 64].

The target is a two-layer thin foil with thickness between 0.1 and 3 μm. The front layer, which accounts for most of the target mass, is made of high-Z material. The rear layer is very thin (0.01–0.1 μm) and it is made of deuterium-containing material. The choice of high-Z–low-Z material is motivated by the observation that if the ratio of mass to charge for the front and rear material is sufficiently large, the light ions from the rear surface are accelerated much more efficiently than the heavy ones [57]. For definitiveness we chose gold as a front layer material, which is a common substance in this kind of high-intensity laser–target interactions. The plasma slab corresponding to this layer has a thickness L_{Au}, density n_{Au} and charge $Z_{Au} - 1$, respectively. For simplicity we assumed that the rear layer is made of pure deuterium with thickness and density L_D and n_D, respectively. Both the front and the rear layers have the form of a disc with a prescribed diameter D_{Au} and D_D, respectively. The geometry of the target is shown in figure 1(*b*). More complex targets in terms of composition and geometry will be modeled in the future. The laser radiation is an ultrashort

pulse of linearly polarized light normally incident on the target. The laser pulse has a spatio-temporal profile $I(y, t) = I_0 \sin^2(\pi t/\tau_0) \exp(-(y/R_0)^2)$ with I_0 being the peak laser intensity, τ_0 the laser pulse duration and R_0 the laser spot radius. The laser propagation direction is $+x$. The simulation box is a rectangle with length L_x (along the laser propagation direction) and width L_y (in the transverse direction). There is a vacuum region in front of the target with a length x_{Au} extending up to several laser wavelengths. A vacuum region of comparable length behind the target is also present. The computational domain is partitioned into a suitable number of grid cells $N_x \times N_y$ with cell size $\Delta x \times \Delta y$, where $\Delta x = L_x/N_x$ and $\Delta y = L_y/N_y$. The cell size is of critical importance. On one hand, it cannot be made too small since for a given number of particles there would be too few particles per cell, which results in poor statistics. On the other hand, too large a cell size may lead to an incorrect solution of the Maxwell equations since the skin depth must be resolved. Therefore, Δx is chosen to be 0.1–0.5 times the skin depth and in most calculations it is 10 nm. The number of particles N_p, used in the PIC model, is typically a few million. The time step Δt was chosen based on the following consideration. We found empirically that the best results are obtained if a particle resides in a given cell for several time steps. This condition may be expressed as $\Delta t \leqslant (1/2)\Delta x/max\{|v_k|\}$, where the denominator is twice the expected maximum velocity of any particle. In the highly relativistic limit this condition reduces to $\Delta t \leqslant \Delta x/2c$, where c is the speed of light.

3. Results and discussions

Electromagnetic PIC simulations are performed for a range of laser and target parameters defined in the previous section. As mentioned in the introduction, we are primarily interested in the conversion efficiency of laser energy into ion kinetic energy and the 'quality' of the ion beam (energy and angular distribution functions), but other related parameters such as mean electron energy and electron energy distribution function will also be discussed. We will commence our analysis with the temporal characteristics of a typical case (section 3.2). In section 3.3 we will vary laser and target parameters in order to derive scaling laws and parameter trends.

3.1. PIC simulation parameters

The peak laser intensity and wavelength for the typical case are $I_0 = 10^{24}$ W m^{-2} and $\lambda_0 = 1\,\mu$m, respectively. The transverse laser profile is a Gaussian with $1/e$ spot size $R_0 = 3\,\mu$m. The laser pulse duration is $\tau_0 = 80$ fs with FWHM $\tau_{FWHM} = \tau_0/2$ of 40 fs (12 cycles) and the input laser energy $E_{laser} = \pi R_0^2 \int_0^{\tau_0} I(0, t')dt' = \pi R_0^2 I_0 \tau_{FWHM}$ is 1.13 J. The computation time is extended to 160 fs, twice the laser pulse duration, since the deuterium ions continue their acceleration after the end of the laser pulse. The target is a highly overdense plasma with density $n_e \cong 100n_c$ ($n_c = 1.12 \times 10^{27}$ m^{-3}—critical electron density). The gold and deuterium layers have thicknesses of 0.25 and 0.05 μm, respectively. The width of both layers is twice the laser spot diameter, e.g. $D_{Au} = D_D = 12\,\mu$m. As the laser intensity drops significantly at the periphery of the target ($\sim$1/50 of that on the axis), the contribution of particles located at $y > 2R_0$ to the energy absorption and ion beam acceleration is small. Doubling the target width was found to have a negligible impact on both the energy absorption and angular distribution of deuterons. Detailed information about the laser and target parameters, as well as some additional simulation parameters, is given in table 1. The laser pulse profile $I(y = 0, t)$ and the unperturbed laser electric field $E_0(y = 0, t)\cos(\omega_0 t)$ on axis with $E_0 = \sqrt{(2I/\varepsilon_0 c)}$ being the envelope of the laser electric field and ω_0 the central

Table 1. Laser, target and computational parameters.

Parameter	Value
Laser peak intensity I_0	$10^{24}\,\mathrm{W\,m^{-2}}$
Laser relativistic parameter a_0	8.5
Laser wavelength λ_0	$1\,\mu\mathrm{m}$
Laser period $T_0 = \lambda_0/c$	$3.33\,\mathrm{fs}$
Laser focal spot radius R_0	$3\,\mu\mathrm{m}$
Laser FWHM τ_{FWHM}	$40\,\mathrm{fs}$
Laser pulse duration τ_0	$80\,\mathrm{fs}$
Front layer $L_{\mathrm{Au}} \times D_{\mathrm{Au}}$	$0.25 \times 12\,\mu\mathrm{m}^2$
Front layer density n_{Au}	$5.8 \times 10^{28}\,\mathrm{m^{-3}}$
Front layer charge $Z_{\mathrm{Au}} - 1$	2
Rear layer $L_{\mathrm{D}} \times D_{\mathrm{D}}$	$0.05 \times 12\,\mu\mathrm{m}^2$
Rear layer density n_{D}	$4.8 \times 10^{28}\,\mathrm{m^{-3}}$
Rear layer charge $Z_{\mathrm{D}} - 1$	1
Computation time T	$160\,\mathrm{fs}$
Simulation box $L_x \times L_y$	$10 \times 20\,\mu\mathrm{m}^2$
Grid cells $N_x \times N_y$	1000×2000
Cell size $\Delta x \times \Delta y$	$10 \times 10\,\mathrm{nm}^2$
Skin depth	$16\,\mathrm{nm}$
Length of vacuum region x_{Au}	$4\,\mu\mathrm{m}$
Number of particles	2×10^6
Time step Δt	$5 \times 10^{-3} T_0$
$c\Delta t/\Delta x$	0.5

laser frequency are given in figure 2. At time $t = 0$ the front of the laser pulse is located at spatial position $x = x_{\mathrm{Au}}$, the vacuum–front layer interface.

3.2. Time-dependent results

In our first example we will focus on the temporal characteristics of the electrons and the ions. One of the main issues of the laser–target interaction process is the absorbed laser energy by the target. When a laser pulse propagates through a solid medium there is an energy loss associated with coupling of the laser electromagnetic wave to the plasma. The absorption of laser energy is plotted in figure 2(c). The solid line is the amount of input laser energy $E_{\mathrm{laser}}(t) = \pi R_0^2 \int_0^t I(0, t')\mathrm{d}t'$, which enters the target from the onset of the laser pulse $t' = 0$ up to time $t' = t$. The other three curves are the energy absorbed by electrons, gold and deuterium ions. They comprise the energy contribution of all particles belonging to the corresponding specie, regardless of their position and direction of motion. The energy absorbed by electrons peaks near the end of the laser pulse and then slightly decreases. The decrease is associated with a transfer of kinetic energy from the electrons to the ions. An additional (unwanted) source of energy loss is the escape of particles from the computational box. At the end of the simulations the electrons have absorbed about ∼0.11 J, gold ions—∼0.15 J and the deuterons—∼0.07 J. The total absorbed energy of ∼0.33 J represents ∼30% of the input laser energy. The conversion efficiency of laser energy into deuteron kinetic energy is ∼6%. The magnitude of the energy absorbed by the front and rear layers, 0.15 J and ∼0.07 J respectively, deserves further elaboration. The front layer is five times thicker compared with the rear layer and contains more atoms. In addition, the laser field decays on a distance of a few skin depths barely reaching the rear layer, therefore depositing electromagnetic energy preferentially in the front layer. But the rear layer has the advantage of having light ions, which are more likely
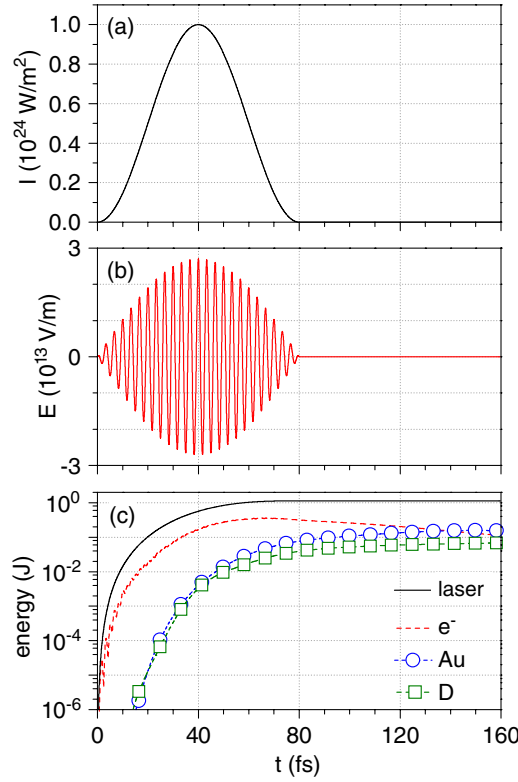
6

Figure 2. Laser pulse intensity (*a*) and laser electric field (*b*) versus time. Absorbed energy by electrons (dashed line), Au^{2+} (open cycles) and D^+ (open squares) and input laser energy (solid line) (*c*) versus time. The laser and target parameters are: $I_0 = 10^{24}\,W\,m^{-2}$, $\lambda_0 = 1\,\mu m$, $R_0 = 3\,\mu m$, $\tau_0 = 80\,fs$, $E_{laser} = 1.13\,J$, $L_{Au} = 0.25\,\mu m$, $L_D = 0.05\,\mu m$, $n_e \cong 100 n_c$. The simulation parameters are listed in table 1.

to be accelerated than the heavy gold ions from the front layer. At these conditions both layers absorb about equal amounts of energy.

Details of the acceleration process are given in figure 3, in which we make a direct comparison of the properties of each species. The top row plots the average energy of the species under consideration. The peak average kinetic energies are comparable, of the order of 1 MeV. The corresponding energy distribution functions are plotted in the next row of figures. For both electrons and ions the energy distribution function is non-Maxwellian, exhibiting a long high-energy tail. The third row of figures plots the average velocities $\langle \vec{v}_\alpha \rangle = (1/N_\alpha) \sum_{n=1}^{N_\alpha} \vec{v}_{k,\alpha}$ of specie $\alpha = e$, Au^{2+}, D^+ along the laser propagation direction x and the transverse direction y. The sum is over all particles k belonging to specie α and N_α is the total number of particles of specie α. Figure 3(*g*) clearly shows strong oscillations of the electrons in the transverse direction, parallel to the laser electric field, with frequency equal to that of the fundamental laser frequency. A small positive push in the laser propagation direction is also observed. The mean velocity $\langle v_{x,e} \rangle$ oscillates with frequency equal to twice the fundamental laser frequency consistent with the $\vec{v} \times \vec{B}$ part of the Lorentz force. The longitudinal ion average velocities look quite different. The magnitude of the average velocity of Au^{2+} is only $\sim 10^5\,m\,s^{-1}$ and the average distance the gold ions can move during the short laser pulse duration of $\sim 10^2$ fs is only $0.01\,\mu m$. Therefore, for all practical purposes the gold ions can be considered immobile on
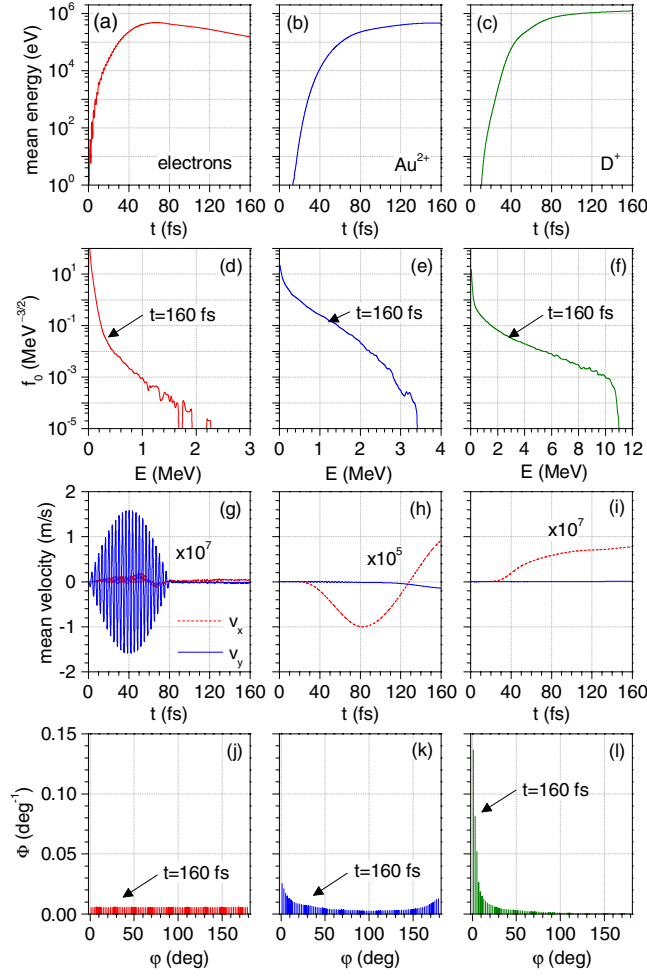
Figure 3. Mean energy of electrons (*a*), Au^{2+} (*b*) and D^+ (*c*); energy distribution function of electrons (*d*), Au^{2+} (*e*) and D^+ (*f*); mean velocity of electrons (*g*), Au^{2+} (*h*) and D^+ (*i*); and angular distribution function of electrons (*j*), Au^{2+} (*k*) and D^+ (*l*). All parameters are as in figure 2.

such a short time scale. It should be kept in mind, however, that they absorb a non-negligible amount of laser energy. The most relevant information regarding the average velocities of ions is illustrated in figure 3(*i*). The deuterons are accelerated to an average velocity approaching $10^7 \, \mathrm{m \, s^{-1}}$, which is $\langle v_{x,D^+} \rangle / c \cong 0.025$ relative to the speed of light. The angular scattering is expressed quantitatively through the angular scattering distribution function $\Phi(\varphi)$, where the angle φ is accounted for from the direction of laser propagation (figures 3(*j*)–(*l*)). The angular distribution function of specie α is constructed by calculating the angle φ_k for each particle k belonging to specie α according to $\varphi_k = |v_{y,k}|/v_{x,k}$ and then making a histogram of the number of counts versus angle bins. The histograms in figure 3 are normalized to unity, i.e. $\int_0^{180} \Phi(\varphi) \mathrm{d}\varphi = 1$. As seen in figure 3(*j*) the electrons are uniformly scattered, while the angular spread of virtually all deuterons lies within a cone of about $20°$ (figure 3(*l*)). The angular scattering of D^+ may be explained from geometrical considerations. The problem is essentially one-dimensional since the aspect ratios for both gold and deuterium layers are
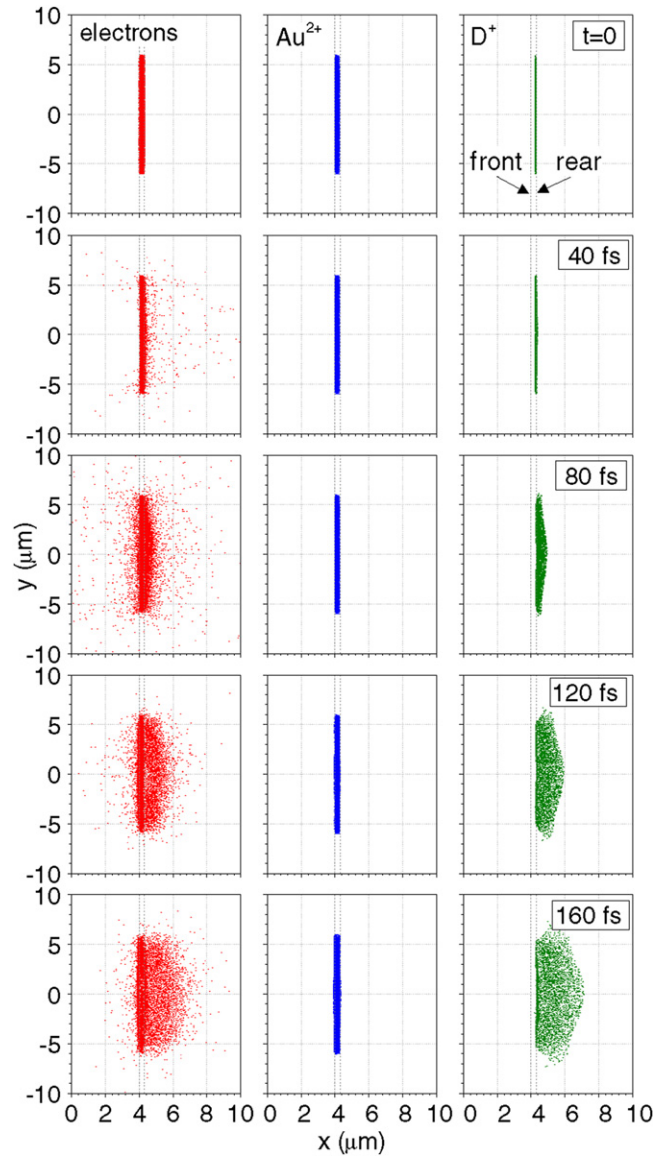
8

Figure 4. Snapshots of particle positions of electrons (left column), Au^{2+} (center column) and D$^+$ (right column). All parameters are as in figure 2.

much smaller than unity ($L_{Au}/D_{Au} \cong 2 \times 10^{-2}$ and $L_D/D_D \cong 4 \times 10^{-3}$, respectively). It is reasonable to expect that the ions will be accelerated in a direction normal to the surface. On the other hand, transverse inhomogeneities of the accelerating electric field cause some small angular spread of the accelerated deuterons.

The main features of electron and ion acceleration are visualized in figure 4, where snapshots of the *xy* positions of the particles are shown. The left column refers to electrons, the middle—to gold ions and the right—to deuterium ions. The first row plots the particle positions at the beginning of the simulations. The second row refers to time $t = 40\,\text{fs}$,

which corresponds to the peak of the laser pulse intensity. At this time no significant particle movement is observed, though there are a few scattered electrons. The next row of figures shows the particle positions at the end of the laser pulse ($t = 80$ fs). We observe electrons scattered both in forward and backward directions. The backward scattered electrons are ejected from the front gold surface. The forward accelerated electrons are a result of the $\vec{v} \times \vec{B}$ component of the Lorentz force pushing the energetic electrons in the direction of laser propagation. It is most effective on axis ($y = 0$), where the magnetic field is strongest. The electrons accelerated forward are relativistic and can reach the rear side of the target. They become separated from the immobile gold ions inducing a space-charge electrostatic field, which accelerates the deuterons. The most energetic deuterons have gained momentum and advanced forward a distance of $\sim 1\,\mu$m. The snapshots of the particle positions at later time $t = 120$ fs and at the end of the simulations $t = 160$ fs show that there is a cloud of blow-off energetic electrons separated from the target and accelerated forward, as well as a cloud of deuterons following these electrons. The latter exhibits a bell-like profile, also observed in [35]. This profile is a result of the radial dependence of the accelerating electrostatic field, which is largest on axis. The electrons (and ions) are preferentially accelerated on the axis and go ahead of those at the periphery, forming the bell-like shape seen in figure 4.

3.3. Variation of the peak laser intensity, laser pulse duration and target thickness

In this section, we describe the general features of deuteron acceleration as a function of peak laser intensity, laser pulse duration and thickness of the front and rear layers. Parametric studies have been performed by others [15, 18, 48, 65–67]. Our analysis is limited to the three most important parameters related to energy absorption by the target: absorbed energy and its distribution among various degrees of freedom, deuteron mean energy and energy conversion efficiency. The deuteron acceleration is then analyzed based on the energy and angular distribution functions. When one of the input parameters is varied (for example, target thickness), all other simulation parameters are kept the same. By 'target thickness' we mean the extent of the front layer. The thickness of the rear layer, usually tens of nanometers, is typically much smaller compared with that of the front layer. This is almost always the case because in actual experiments the light ions (H$^+$) are just contaminants residing on the back surface of the target.

We commence with variation of the target thickness. To understand the incentives of studying the variation of this parameter, let us compare two commonly used targets in laser–target interactions: clusters and solids. Clusters are tiny targets at solid density, only a few nanometers in diameter. Extensive studies during the last ten years revealed that the ion kinetic energy of exploding clusters increases dramatically with cluster diameter (which, for simplicity, may be attributed to as 'target thickness') [68]. On the other hand, when the target becomes a few micrometer thick, the energy of the light ions decreases with target thickness increasing as shown by MacKinnon *et al* [41]. Apparently, the peak ion energy is expected to reach a maximum somewhere in between. The first series of simulations, in which the target thickness is varied between 0.1 and 3 μm, is plotted in figure 5, left column. We observe two distinct cases of target thickness. Very thin front layer $L_{\text{Au}} \leqslant 0.5\,\mu$m provides efficient energy absorption (figure 5(*a*)), high deuteron mean ion energy ~ 1 MeV (figure 5(*e*)) and significant energy conversion efficiency of a few percent (figure 5(*i*)). The energy conversion efficiency η_D is defined as the energy absorbed by D$^+$ divided by the input laser energy. Targets with thickness $L_{\text{Au}} \geqslant 0.5\,\mu$m lead to a precipitous drop of both the mean energy and energy conversion efficiency of D$^+$. The reason becomes apparent when examining the specie energy absorption plotted in figure 5(*a*). For the thickest target considered ($L_{\text{Au}} = 3\,\mu$m) the
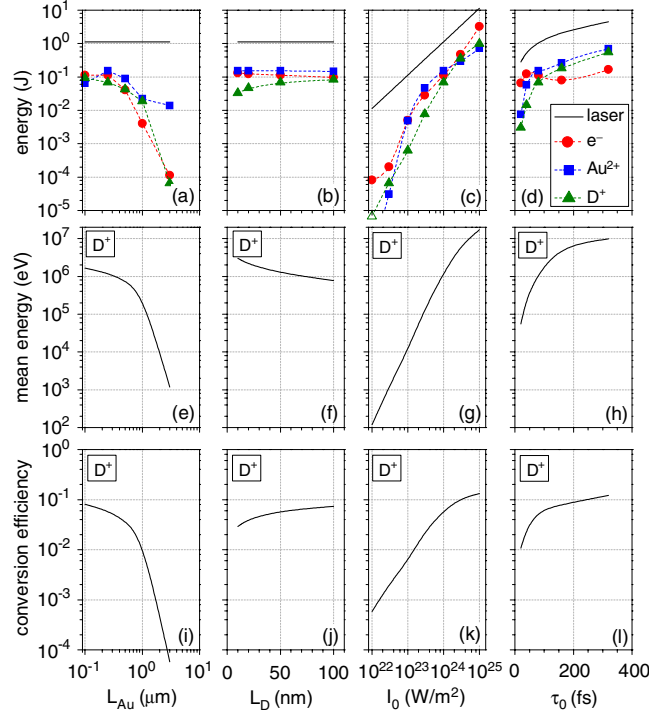
Figure 5. Laser and absorbed energy (*a*)–(*d*); mean energy (*e*)–(*h*) and energy conversion efficiency of D$^+$ (*i*)–(*l*) as a function of target thickness (left column), D layer thickness (second column), peak laser intensity (third column) and laser pulse duration (right column).

bulk of the absorbed energy ($\sim$99%) goes to the ions of the front layer, while the deuterons absorb only a tiny fraction of the laser energy, about 0.01%. The 'critical target thickness', separating the two regimes, can be compared with the skin depth L_{skin}. At these conditions the relativistic skin depth is $\sim$0.15 μm, approximately one-third of the 'critical target thickness'. If the target thickness greatly exceeds the skin depth, i.e. $L_{Au} \gg L_{skin}$, the laser field is exponentially attenuated inside the front layer and cannot penetrate deep enough to reach the rear layer, leading to a decline of the mean deuteron energy and energy conversion efficiency. The position of the fall-off depends upon the skin depth, which, in turn, depends upon the electron density. If the electron density was lower, say $n_e \cong 10n_c$, the skin depth would be larger and the fall-off would occur for larger target thicknesses. Our simulation results agree well with published data [41], which show a rapid fall-off of the mean ion energy with the target thickness increasing. The results in figures 5(*e*) and (*i*) do not indicate an optimum target thickness (none of the studied parameters goes through a maximum). The reason is again the assumed plasma density of the front layer. Studies have shown that the optimum target thickness scales inversely with the target plasma density [48] and in our case the plasma is highly overdense ($n_e \cong 100n_c$). According to figure 20(*b*) from [48] at $n_c/n_e \cong 0.01$ the optimum target thickness is expected to be 0.05 μm, which is below the thickness range plotted in figure 5. In order to compare with the data in [48] we repeated the simulations with $n_e \cong 20n_c$. We observed a broad peak for both the mean deuteron energy and energy conversion efficiency located between $L_{Au} = 0.1$ and 0.25 μm, which agrees well with the value $L_{Au} = 0.25$ μm derived from the same figure. The thickness of the deuterium layer

11

may also be significant. For a given laser energy $E_{\text{laser}} = \pi R_0^2 I_0 \tau_0 / 2$ and energy conversion efficiency η_D the mean ion energy is $\langle u_{D^+} \rangle = \eta_D E_{\text{laser}} / N_D$, where $N_D = \pi R_0^2 L_D n_D$ is the number of deuterium ions. After simple manipulations one readily derives

$$\langle u_{D^+} \rangle = \eta_D \frac{F_0}{n_D L_D}. \tag{2}$$

The nominator is the laser fluence $F_0 = E_{\text{laser}} / (\pi R_0^2) = I_0 \tau_0 / 2$ (laser energy per unit area) in units J m^{-2}, while the denominator contains the thickness of the deuterium layer. Formula (2) implies that the average deuteron energy depends on two parameters, the laser fluence and the deuterium layer thickness, provided the conversion efficiency η_D is reasonably constant over a range of parameters. For fixed laser parameters this is true for relatively thin targets, $L_{\text{Au}} \ll 0.5 \, \mu$m, comparable to the plasma skin depth. Higher deuteron energy can be achieved by using either a laser with higher fluence (decreasing, if possible, the laser spot size R_0) or a thinner deuterium-containing layer. The latter expresses the fact that the energy absorbed by the deuterium layer is spread over fewer deuterons, allowing them to gain higher mean average energy. Indeed, simulations with thickness of the deuterium layer $L_D = 0.1, 0.05, 0.02$ and $0.01 \, \mu$m confirm the upward trend of the mean deuteron energy with L_D decreasing (figure 5(f)). It should be kept in mind, however, that there is a drawback of making the deuterium layer too thin; it results in acceleration of fewer deuterons.

The third and fourth columns in figure 5 plot the same parameters versus peak laser intensity and laser pulse duration, respectively. As expected, both the energy conversion efficiency and the mean energy of D$^+$ increase with peak laser intensity and pulse duration. For peak laser intensities approaching $I_0 = 10^{25}$ W m^{-2} the conversion efficiency saturates and the mean deuteron energy increases primarily due to the increase of the peak laser intensity. The conversion efficiency versus laser pulse durations shows two distinct regimes (figure 5(l)). It increases exponentially for $\tau_0 < 100$ fs, indicating that the time is not sufficient to accelerate the ions. For $\tau_0 > 100$ fs the moderate increase with τ_0 suggests that the ions have been sufficiently accelerated to their maximum velocity. Very long laser pulse duration, however, is to be avoided in order to prevent Au ions from being accelerated, aiming at depositing a larger fraction of the laser energy into the light ions.

Figures 6 to 9 address the main deuteron beam parameters, the energy and angular distribution functions of D$^+$. They were studied by varying the same laser and target parameters (one at a time) as in figure 5. The effect of the target thickness is seen in figure 6. The energy distribution function is bi-Maxwellian, having a bulk of cold ions and a long tail, which extends to kinetic energy of several MeV. For $L_{\text{Au}} = 0.1 \, \mu$m ions with kinetic energy of up to 15 MeV are observed. With increasing target thickness the maximum ion energy decreases. The decrease is most dramatic for target thickness between 1 and 3 μm. The angular distribution function of D$^+$ is also target thickness sensitive. For $L_{\text{Au}} < 1 \, \mu$m the angular distribution function peaks at very small scattering angle. With increasing target thickness the scattering becomes more isotropic. From figures 5 and 6 we conclude that very thin targets, of the order of or less than 1 μm (for $n_e \cong 100 n_c$), favour the generation of energetic and forward accelerated ions. The thickness of the deuterium layer has little impact on the deuteron distribution function (figure 7, left). It has a profound effect, however, on the angular scattering of the deuterons. The thinner the deuterium layer, the narrower the angular distribution becomes (figure 7, right). Therefore, it is advantageous to prepare targets with a very thin (10–50 nm) layer of deuterium-containing material.

The next sequence of figures illustrates the ion acceleration versus input laser parameters. The deuteron energy and angular distribution function for four peak laser intensities varying from $I_0 = 10^{22}$ to $I_0 = 10^{25}$ W m^{-2} are plotted in figure 8. As expected, the maximum
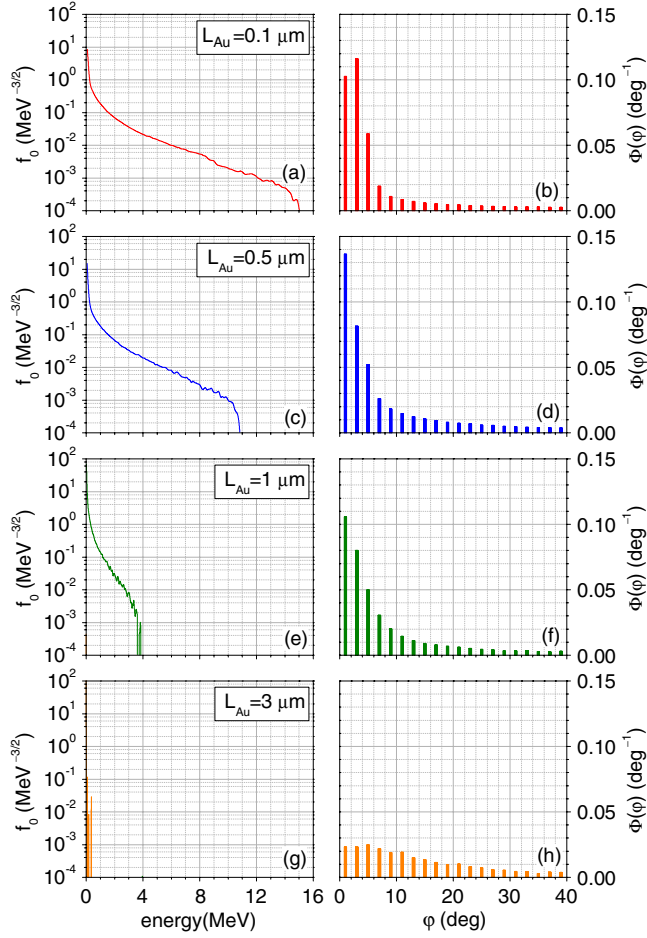
Figure 6. Deuteron energy distribution function (left column) and angular distribution function (right column) for different target thicknesses. All parameters, except the target thickness, are as in figure 2.

ion energy increases with peak laser intensity, following approximately a linear dependence. For peak laser intensity equal to or below $I_0 = 10^{24} \, \mathrm{W \, m^{-2}}$ the ion distribution function is bi-Maxwellian. But for the highest peak laser intensity of $I_0 = 10^{25} \, \mathrm{W \, m^{-2}}$ an ion beam with broad energy spectrum between 2 and 50 MeV is formed. The laser pulse duration affects only the ion energy, but not the angular distribution (figure 9). The ions attain higher energy with the pulse duration increasing simply because more laser energy is deposited and because the ions are accelerated for a longer period of time. These results naturally pose the question, whether the deuteron acceleration depends on the peak laser intensity and pulse duration separately, or on the combination of both. We chose as universal parameter the laser fluence $F_0 = I_0 \tau_0 / 2$, following the derivation of equation (2). In figure 10 we plot the deuteron mean energy and conversion efficiency versus laser fluence. The solid curve refers to variation of the peak laser intensity, while the dashed curve with symbols refers to variation of the laser pulse duration. Not only do both curves exhibit similar trends but they are also quantitatively similar. We can conclude that the properties of the deuteron beam depend on the laser fluence rather than the input laser intensity and pulse duration separately.
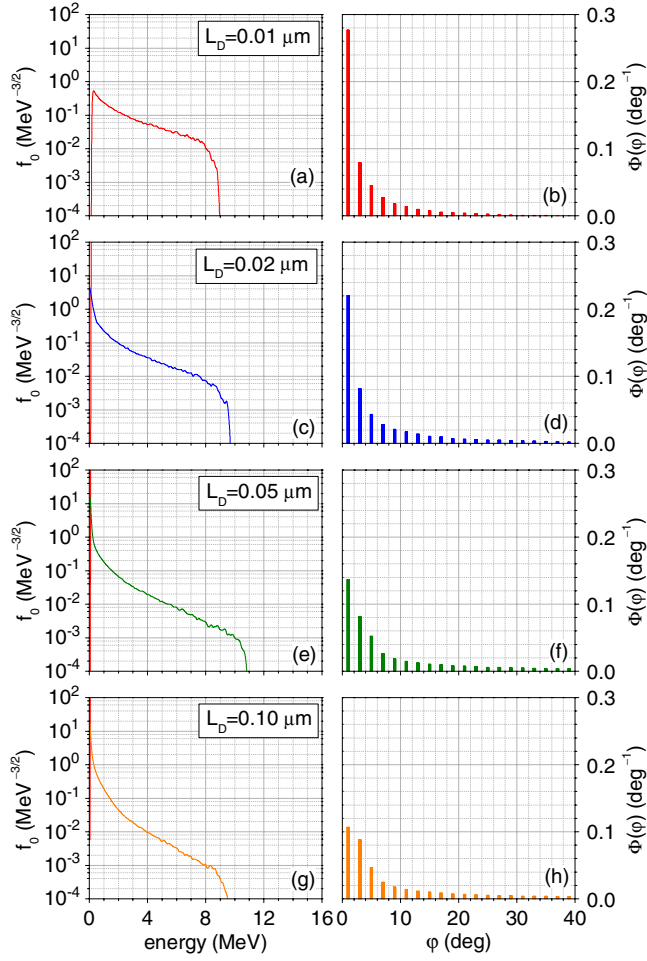
Figure 7. Deuteron energy distribution function (left column) and angular distribution function (right column) for different thicknesses of the D layer. All parameters, except the thickness of the D layer, are as in figure 2.

3.4. Comparison with other simulations

Benchmarks of simulation results are always essential to validate a model. A one-to-one comparison is highly desirable, but often difficult to do, especially at the extreme conditions prevalent here. Either the laser or target parameters may not be exactly matched. In this case, we deal with deuterium and the data for deuteron acceleration is scarce. The available data are mostly for uniform (not layered) targets [33–35]. Therefore, due to the lack of adequate data, we compare deuteron with proton acceleration. This is not too restrictive since the mechanism of light ion acceleration from the rear surface of the target via TNSA is very general and can be applied to ions with comparable charge-to-mass ratio. Proton acceleration has been extensively studied and there is a wealth of data published in the literature. For example, Esirkepov *et al* [52] have done extensive parametric study of proton acceleration from a double-layer target for laser and target parameters, which are similar to our calculations. The thickness of the front and rear layers are the same, $1\,\mu$m and $0.06\,\mu$m, respectively, and the plasma is
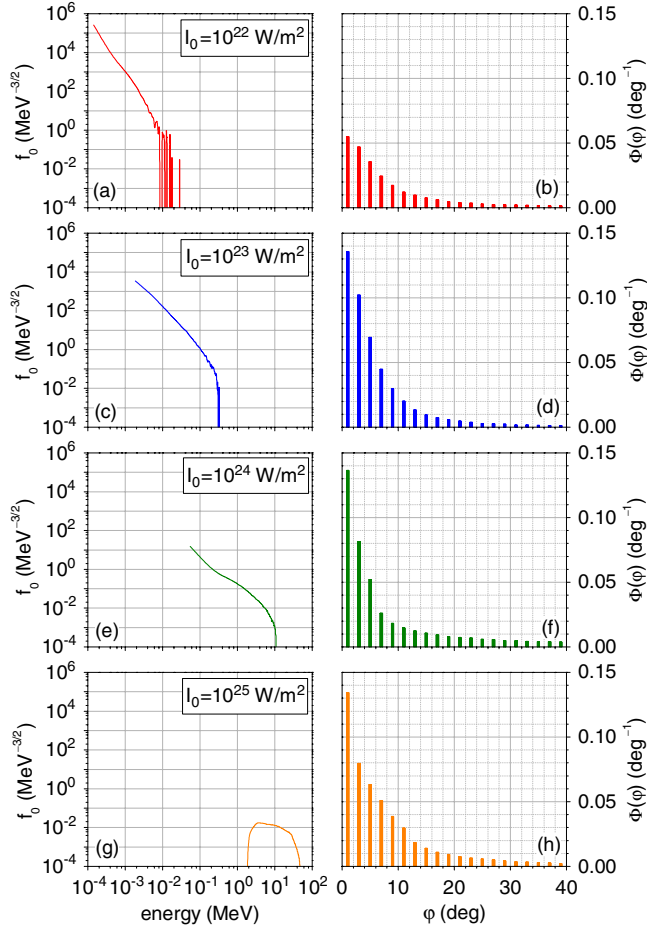
14

Figure 8. Deuteron energy distribution function (left column) and angular distribution function (right column) for different peak laser intensities. All parameters, except the peak laser intensity, are as in figure 2.

equally overdense, $n_e \cong 100n_c$. The data in figure 3 from [52] plot the maximum ion energy versus input laser energy and cover the variation of a wide range of peak laser intensities, pulse duration and laser spot size. We selected a subset of these data for laser beam diameters $10\,\mu m$ and $25\,\mu m$ ($R_0 = 5$ and $12.5\,\mu m$). We then converted the laser energy to fluence by dividing it to the area of the corresponding laser spot (πR_0^2). Our simulations (solid line) and the data from [52] (symbols) are shown in figure 11, where the maximum ion energy is plotted versus laser fluence. The agreement is very good, keeping in mind that our simulations are for deuterons, while that in [52] are for protons. The data by Esirkepov *et al* [52] for different peak laser intensities, pulse duration and laser spot size also confirm what we found in the previous sub-section, namely that for sub-micrometer targets the main factor governing the ion acceleration is the laser fluence.

4. Conclusion

Numerical simulations using a 2D electromagnetic PIC model of deuteron acceleration in high-intensity laser thin-foil interaction have been presented. Our study investigates the effect
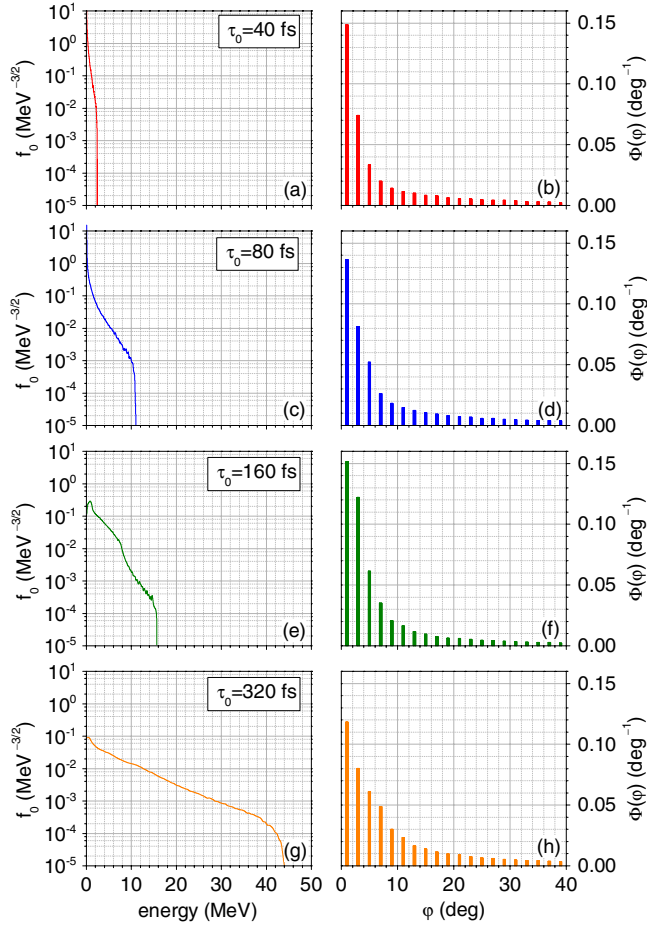
Figure 9. Deuteron energy distribution function (left column) and angular distribution function (right column) for different laser pulse durations. All parameters, except the laser pulse duration, are as in figure 2.

of target thickness, peak laser intensity and laser pulse duration on the ion energy and angular distribution functions and conversion efficiency of laser energy into ion kinetic energy for highly overdense plasma $n_e/n_c \cong 100$. Our findings can be summarized as follows:

(i) With increasing peak laser intensity or laser pulse duration the average deuteron energy and conversion efficiency of laser energy into kinetic energy of the deuterons increase. Both the average deuteron energy and the conversion efficiency of laser energy into kinetic energy of the deuterons depend essentially on the laser fluence rather than the peak intensity and pulse duration separately.

(ii) The average deuteron energy and conversion efficiency of laser energy into kinetic energy of the deuterons decrease as the target thickness increases. With the increasing target thickness the angular scattering of the deuterons becomes more uniform. Decreasing the target thickness improves the angular collimation of D⁺.

(iii) The thickness of the deuterium layer affects the angular spread of deuterons. The ion beam collimation improves with the decreasing deuterium layer thickness.
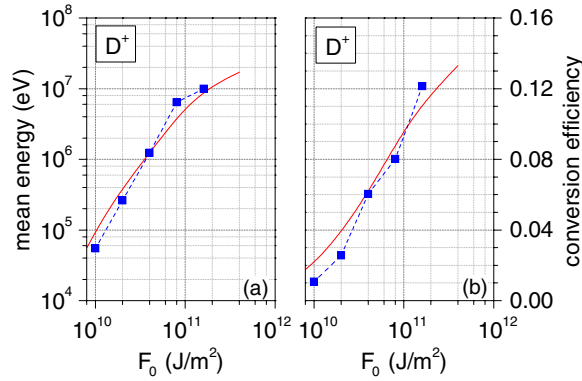
16

Figure 10. Deuteron mean energy (*a*) and energy conversion efficiency versus laser fluence (*b*). Solid line—variation of the peak laser intensity for constant laser pulse duration, symbols—variation of the laser pulse duration for constant peak laser intensity.
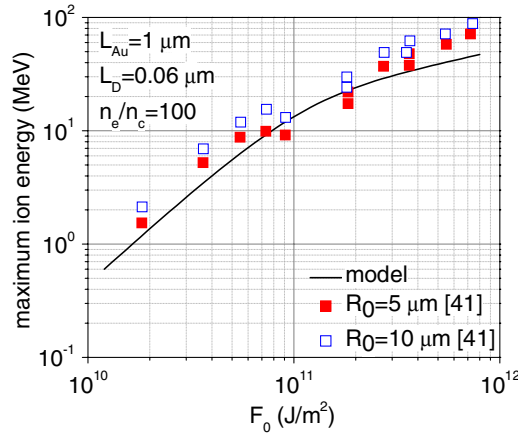
Figure 11. Deuteron and proton maximum kinetic energy versus laser fluence. Solid line—model: $\lambda_0 = 1\,\mu$m, $L_{Au} = 1\,\mu$m, $L_D = 0.06\,\mu$m, $n_e \cong 100n_c$, $R_0 = 3\,\mu$m. Symbols: $\lambda_0 = 1\,\mu$m, $L_{Au} = 1\,\mu$m, $L_H = 0.06\,\mu$m, $n_e \cong 100n_c$, $R_0 = 5\,\mu$m (closed symbols), $R_0 = 12.5\,\mu$m (open symbols) [52]. The solid line refers to D^+, while the symbols are for H^+.

(iv) The deuterons are accelerated in the forward direction by TNSA for $I_0 > 10^{23}\,\mathrm{W\,m^{-2}}$ and $L_{Au} < 1\,\mu$m.

The simulation results demonstrate that a well-collimated relativistic beam of deuterons can be produced in laser–thin foil interaction, which can serve as a precursor for generation of a high-flux neutron beam. These data will be used as input parameters of a model simulating the production and scattering of the neutrons.

Appendix

The problem modeled is studied in a 2D Cartesian coordinate system. There is no variation in the z direction, i.e. $\partial/\partial z = 0$ for all variables. We consider a TE electromagnetic wave propagating in the $+x$ direction with field components $\vec{E} = (E_x(x, y),\ E_y(x, y), 0)$, $\vec{H} = (0, 0,\ H_z(x, y))$ and $\vec{B} = \mu_0 \vec{H}$. With these assumptions the Maxwell equations takes the forms

$$\frac{\partial E_x}{\partial t} = \frac{1}{\varepsilon_0}\left(\frac{\partial H_z}{\partial y} - j_x\right), \tag{1a}$$

$$\frac{\partial E_y}{\partial t} = \frac{1}{\varepsilon_0}\left(-\frac{\partial H_z}{\partial x} - j_y\right), \tag{1b}$$

$$\frac{\partial H_z}{\partial t} = \frac{1}{\mu_0}\left(\frac{\partial E_x}{\partial y} - \frac{\partial E_y}{\partial x}\right), \tag{1c}$$

with $\vec{j} = (j_x(x, y), j_y(x, y), 0)$ being the conduction current density. The relativistic equations of motion of a charged particle α in an electromagnetic field is described by the following set of equations:

$$\frac{\mathrm{d}\vec{p}_\alpha}{\mathrm{d}t} = q_\alpha\left(\vec{E} + \frac{\vec{p}_\alpha}{m_\alpha \gamma_\alpha} \times \vec{B}\right), \tag{2a}$$

$$\vec{v}_\alpha = \frac{\vec{p}_\alpha/m_\alpha}{\sqrt{1 + (\vec{p}_\alpha/m_\alpha c)^2}}, \tag{2b}$$

$$\frac{\mathrm{d}\vec{x}_\alpha}{\mathrm{d}t} = \vec{v}_\alpha, \tag{2c}$$

where $\vec{p}_\alpha = (p_{\alpha,x}(x, y), p_{\alpha,y}(x, y), 0)$, $\vec{v}_\alpha = (v_{\alpha,x}(x, y), v_{\alpha,y}(x, y), 0)$, m_α and q_α are the particle relativistic momentum, velocity, mass and charge, respectively, and $\gamma_\alpha = \sqrt{1 + (\vec{p}_\alpha/m_\alpha c)^2}$ is the relativistic factor. Equation (2a) is discretized to form two FD equations for the impulse components with a solution

$$p_{\alpha,x}^{n+1} = \frac{q_\alpha E_x^{n+1/2}\Delta t + \eta_\alpha^{n+1/2} q_\alpha E_y^{n+1/2}\Delta t + \left(1 - (\eta_\alpha^{n+1/2})^2\right)p_{\alpha,x}^n + 2\eta_\alpha^{n+1/2} p_{\alpha,y}^n}{1 + (\eta_\alpha^{n+1/2})^2}, \tag{3a}$$

$$p_{\alpha,y}^{n+1} = \frac{q_\alpha E_y^{n+1/2}\Delta t - \eta_\alpha^{n+1/2} q_\alpha E_x^{n+1/2}\Delta t + \left(1 - (\eta_\alpha^{n+1/2})^2\right)p_{\alpha,y}^n - 2\eta_\alpha^{n+1/2} p_{\alpha,x}^n}{1 + (\eta_\alpha^{n+1/2})^2}. \tag{3b}$$

The dimensionless parameter $\eta_\alpha^{n+1/2} = (q_\alpha B_z^{n+1/2}/2m_\alpha \gamma_\alpha^{n+1/2})\Delta t$ is the cyclotron frequency times the time step. The superscript denotes quantities at the corresponding time level. The current density at the new time level $\vec{j}_\alpha^{n+1} \equiv n_\alpha q_\alpha \vec{v}_\alpha^{n+1}$ is calculated by multiplying (3) by the factor $n_\alpha q_\alpha/m_\alpha \gamma_\alpha^{n+1}$. Second-order correct discretization of equations (1a)–(1c) mandates the current density in the Maxwell equations to be calculated at half time steps, which we do by averaging over t_n and t_{n+1}, $\vec{j}_\alpha^{n+1/2} = (\vec{j}_\alpha^{n+1} + \vec{j}_\alpha^n)/2$. The expression for the x and y components of $\vec{j}_\alpha$ takes the forms

$$j_{\alpha,x}^{n+1/2} = a_\alpha^{n+1/2} E_x^{n+1/2} + b_\alpha^{n+1/2} E_y^{n+1/2} + \Delta j_{\alpha,x}^n, \tag{4a}$$

$$j_{\alpha,y}^{n+1/2} = a_\alpha^{n+1/2} E_y^{n+1/2} - b_\alpha^{n+1/2} E_x^{n+1/2} + \Delta j_{\alpha,y}^n, \tag{4b}$$

where

$$\Delta j_{\alpha,x}^{n} = \frac{j_{\alpha,x}^{n} + \eta_{\alpha}^{n+1/2} j_{\alpha,y}^{n}}{1 + (\eta_{\alpha}^{n+1/2})^2}, \qquad \Delta j_{\alpha,y}^{n} = \frac{j_{\alpha,y}^{n} - \eta_{\alpha}^{n+1/2} j_{\alpha,x}^{n}}{1 + (\eta_{\alpha}^{n+1/2})^2},$$

$$a_{\alpha}^{n+1/2} = \frac{n_{\alpha} q_{\alpha}^2 \Delta t}{2 m_{\alpha} \gamma_{\alpha}^{n+1/2} \left(1 + (\eta_{\alpha}^{n+1/2})^2\right)}$$

and $b_{\alpha}^{n+1/2} = \eta_{\alpha}^{n+1/2} a_{\alpha}^{n+1/2}$. The global current density $\vec{j} = \sum_{\alpha} \vec{j}_{\alpha}$ is computed by adding the current densities of individual particles:

$$j_x(\vec{r}) = a(\vec{r}) E_x(\vec{r}) + b(\vec{r}) E_y(\vec{r}) + \Delta j_x(\vec{r}), \tag{5a}$$

$$j_y(\vec{r}) = a(\vec{r}) E_y(\vec{r}) - b(\vec{r}) E_x(\vec{r}) + \Delta j_y(\vec{r}). \tag{5b}$$

The coefficients are calculated on grid nodes $\vec{r}$ by summing the coefficients of individual particles times the particle shape function. The key issue is to collect (and interpolate) the coefficients, rather than the current density itself. Equations (5a) and (5b) are written in such a fashion, that the electric field is *factored out*. Inserting (5a) and (5b) into the Maxwell equations (1a)–(1c) and transferring the terms with the electric field into the left-hand side we get

$$\frac{\partial E_x}{\partial t} + \frac{a}{\varepsilon_0} E_x + \frac{b}{\varepsilon_0} E_y = \frac{1}{\varepsilon_0} \left(\frac{\partial H_z}{\partial y} - \Delta j_x \right), \tag{6a}$$

$$\frac{\partial E_y}{\partial t} + \frac{a}{\varepsilon_0} E_y - \frac{b}{\varepsilon_0} E_x = \frac{1}{\varepsilon_0} \left(-\frac{\partial H_z}{\partial x} - \Delta j_y \right), \tag{6b}$$

$$\frac{\partial H_z}{\partial t} = \frac{1}{\mu_0} \left(\frac{\partial E_x}{\partial y} - \frac{\partial E_y}{\partial x} \right). \tag{6c}$$

Solving (6a)–(6c) is advantageous compared with solving the original equations (1a)–(1c). The leading coefficient a is non-negative and changes on a time scale, much longer than a laser cycle. The system of two linear equations for E_x and E_y has a determinant that is always positive due to the particular arrangement of the coefficients a and b. As a consequence, the system of equations (6a)–(6c) is very robust and efficient in dumping spurious solutions.

Equations (6a)–(6c) require initial and boundary conditions. At the beginning of the computations the electromagnetic field components are set to zero. To allow outgoing electromagnetic waves to leave the computational domain without spurious reflections from the edges, we use boundary conditions [69]

$$\left(\frac{\partial}{\partial t} - c \frac{\partial}{\partial x} \right) Y = 0, \qquad x = 0, \tag{7a}$$

$$\left(\frac{\partial}{\partial t} + c \frac{\partial}{\partial x} \right) Y = 0, \qquad x = L_x, \tag{7b}$$

$$\left(\frac{\partial}{\partial t} - c \frac{\partial}{\partial y} \right) Y = 0, \qquad y = -L_y/2, \tag{7c}$$

$$\left(\frac{\partial}{\partial t} + c \frac{\partial}{\partial y} \right) Y = 0, \qquad y = L_y/2, \tag{7d}$$

where $Y = E_x, E_y$. There are no boundary conditions for H_z: it is calculated directly from (6c). Equations (6a)–(6c) also require a 'source field' located at the left boundary $x = 0$. For

each time step boundary conditions ($7a$)–($7d$) are applied and then E_y is updated according to [70]:

$$E_y(y, t) \rightarrow E_y(y, t) - 2\omega_0 \Delta t E_0(y, t) \sin(\omega_0 t), \qquad (8)$$

where $E_0(y, t) = \sqrt{2I(y,t)/c\varepsilon_0}$ is the envelope of the unperturbed laser electric field. The source electric field is, in fact, twice the time derivative of the driver laser field $E_0(y, t) \cos(\omega_0 t)$. Note that in this discretization scheme the field components and the current density are located on grid nodes, which is different from the arrangement in the conventional Yee algorithm.

References

[1] Ledingham K W D 2006 *Hyperfine Interact.* **171** 69
[2] Ma C M, Veltchev I, Fourkal E, Li J S, Luo W, Fan J, Lin T and Pollack A 2006 *Laser Phys.* **16** 639
[3] Ledingham K W D, McKenna P and Singhal R P 2003 *Science* **300** 1107
[4] Salamin Y I, Hu S X, Hatsagortsyan K Z and Keitel C H 2006 *Phys. Rep.* **427** 41
[5] Lancaster K L *et al* 2004 *Phys. Plasmas* **11** 3404
[6] Magill J, Galy J and Zagar T 2006 *Lecture Notes Phys.* **694** 131
[7] Perkins L J, Logan B G, Rosen M D, Perry M D, Diaz de la Rubia T, Ghoniem N M, Ditmire T, Springer P T and Wilks S C 2000 *Nucl. Fusion* **40** 1
[8] Krushelnick K, Clark E L, Beg F N, Dangor A E, Najmudin Z, Norreys P A, Wei M and Zepf M 2005 *Plasma Phys. Control. Fusion* **47** B451
[9] Wei M S *et al* 2004 *Phys. Rev. Lett.* **93** 155003
[10] Ditmire T, Zweiback J, Yanovsky V P, Cowan T E, Hays G and Wharton K B 1999 *Nature (London)* **398** 489
[11] Buersgens F, Madison K W, Symes D R, Hartke R, Osterhoff J, Grigsby W, Dyer G and Ditmire T 2006 *Phys. Rev.* E **74** 016403
[12] Zweiback J 2002 *Phys. Plasmas* **9** 3108
[13] Petrov G M, Davis J and Velikovich A L 2006 *Plasma Phys. Control. Fusion* **48** 1721
[14] Badziak J, Woryna E, Parys P, Platonov K Yu, Jablonski S, Ryc L, Vankov A B and Wolowski J 2003 *Nuclear Instrum Metods. Phys. Res.* A **498** 503
[15] Borghesi M, Fuchs J, Bulanov S V, Mackinnon A J, Patel P K and Roth M 2006 *Fusion Sci. Technol.* **49** 412
[16] Wilks S C, Langdon A B, Cowan T E, Roth M, Singh M, Hatchett S, Key M H, Pennington D, MacKinnon A and Snavely R A 2001 *Phys. Plasmas* **8** 542
[17] McKenna P, Ledingham K W D and Robson L 2006 *Lecture Notes Phys.* **694** 91
[18] Sentoku Y, Cowan T E, Kemp A and Ruhl H 2003 *Phys. Plasmas* **10** 2009
[19] Yin L, Albright B J, Hegelich B M, Bowers K J, Flippo K A, Kwan T J T and Fernandez J C 2007 *Phys. Plasmas* **14** 056706
[20] Silva L O, Marti M, Davies J R and Fonseca R A 2004 *Phys. Rev. Lett.* **92** 015002
[21] Esirkepov T, Borghesi M, Bulanov S V, Mourou G and Tajima T 2004 *Phys. Rev. Lett.* **92** 175003
[22] Yang J M *et al* 2004 *J. Appl. Phys.* **96** 6912
[23] Lancaster K L *et al* 2004 *Phys. Plasmas* **11** 3404
[24] Norreys P A, Fews A P, Beg F N, Bell A R, Dangor A E, Lee P, Nelson M B, Schmidt H, Tatarakis M and Cable M D 1998 *Plasma Phys. Control. Fusion* **40** 175
[25] Disdier L, Garconnet J-P, Malka G and Miquel J-L 1999 *Phys. Rev. Lett.* **82** 1454
[26] Youssef A, Kodama R, Habara H, Tanaka K A, Sentoku Y, Tampo M and Toyama Y 2005 *Phys. Plasmas* **12** 110703
[27] Izumi N *et al* 2002 *Phys. Rev.* E **65** 036413
[28] Hilscher D, Berndt O, Enke M, Jahnke U, Nickles P V, Ruhl H and Sandner W 2001 *Phys. Rev.* E **64** 016414
[29] Santala M I K, Zepf M, Beg F N, Clark E L, Dangor A E, Krushelnick K, Tatarakis M and Watts I 2001 *Appl. Phys. Lett.* **78** 19
[30] Pretzler G *et al* 1998 *Phys. Rev.* E **58** 1165
[31] Habara H *et al* 2004 *Phys. Rev.* E **70** 046414
[32] Shen B, Zhang X and Yu M Y 2005 *Phys. Rev.* E **71** 015401(R)
[33] Toupin C, Lefebvre E and Bonnaud G 2001 *Phys. Plasmas* **8** 1011
[34] Macchi A 2006 *Appl. Phys.* B **82** 337

[35] Macchi A, Cattani F, Liseykina T V and Cornolti F 2006 Superstrong fields in plasmas *3rd Int. Conf. on Superstrong Fields in Plasmas* ed D Batani and M Lontano (American Institute of Physics) Conf. Proc. vol 827 p 215

[36] Pukhov A and Meyer-ter-Vehn J 1998 *Phys. Plasmas* **5** 1880

[37] Lasinski B F, Langdon A B, Hatchett S P, Key M H and Tabak M 1999 *Phys. Plasmas* **6** 2041

[38] Ueshima Y, Sentoku Y and Kishimoto Y 2000 *Nuclear Instrum. Methods Phys. Res.* A **455** 181

[39] Sentoku Y *et al* 2000 *Phys. Rev.* E **62** 7271

[40] Murakami Y, Kitagawa Y, Sentoku Y, Mori M, Kodama R, Tanaka K A, Mima K and Yamanaka T 2001 *Phys. Plasmas* **8** 4138

[41] MacKinnon A J, Sentoku Y, Patel P K, Price D W, Hatchett S, Key M H, Andersen C, Snavely R and Freeman R R 2002 *Phys. Rev. Lett.* **88** 215006

[42] Sentoku Y, Bychenkov V Y, Flippo K, Maksimchuk A, Mima K, Mourou G, Sheng Z M and Umstadter D 2002 *Appl. Phys.* B **74** 207

[43] Matsukado E *et al* 2003 *Phys. Rev. Lett.* **91** 215001

[44] Habara K *et al* 2004 *Phys. Rev.* E **70** 046414

[45] Andreev A A, Okada T, Platonov K Yu and Toraya S 2004 *Laser Part. Beams* **22** 431

[46] Miyazaki S, Kawata S, Sonobe R and Kikuchi T 2005 *Phys. Rev.* E **71** 056403

[47] Macchi A, Cattani F, Liseykina T V and Cornolti F 2005 *Phys. Rev. Lett.* **94** 165003

[48] d'Humières E, Lefebvre E, Gremillet L and Malka V 2005 *Phys. Plasmas* **12** 062704

[49] Okada T, Mikado Y, Kitada T, Sugie M and Andreev A A 2005 *Japan. J. Appl. Phys.* **44** 1431

[50] Okada T, Andreev A A, Mikado Y and Okubo K 2006 *Phys. Rev.* E **74** 026401

[51] Okada T, Mikado Y and Okubo K 2006 *J. Plasma Phys.* **72** 1273

[52] Esirkepov T, Yamagiwa M and Tajima T 2006 *Phys. Rev. Lett.* **96** 105001

[53] He F, Xu H, Tian Y, Yu W, Lu P and Li R 2006 *Phys. Plasmas* **13** 073102

[54] Antici P *et al* 2007 *Phys. Plasmas* **14** 030701

[55] Velchev I, Fourkal E and Ma C-M 2007 *Phys. Plasmas* **14** 033106

[56] Kemp A J, Fuchs J, Sentoku Y, Sotnikov V, Bakeman M, Antici P and Cowan T E 2007 *Phys. Rev.* E **75** 056401

[57] Esirkepov T *et al* 2002 *Phys. Rev. Lett.* **89** 175003

[58] Pukhov A 2001 *Phys. Rev. Lett.* **86** 3562

[59] Sentoku Y, Mima K, Sheng Z M, Kaw P, Nishihara K and Nishikawa K 2002 *Phys. Rev.* E **65** 046408

[60] Sentoku Y, Mima K, Ruhl H, Toyama Y, Kodama R and Cowan T E 2004 *Phys. Plasmas* **11** 3083

[61] Okada T, Ogawa K and Sugie M 2006 *J. Plasma Phys.* **72** 925

[62] Welch D R, Rose D V, Cuneo M E, Campbell R B and Mehlhorn T A 2006 *Phys. Plasmas* **13** 063105

[63] Mason R J 1987 *J. Comput. Phys.* **71** 429

[64] Ricci P, Lapenta G and Brackbill J U 2002 *J. Comput. Phys.* **183** 117

[65] Fuchs J *et al* 2006 *Nature Phys.* **2** 48

[66] Robson L *et al* 2006 *Nature Phys.* **3** 58

[67] Oishi Y *et al* 2005 *Phys. Plasmas* **12** 073102

[68] Petrov G M, Davis J, Velikovich A L, Kepple P, Dasgupta A and Clark R W 2005 *Phys. Plasmas* **12** 063103

[69] Taflove A and Hagness S C 2005 *Computational Electrodynamics: The Finite-Difference Time-Domain Method* (Boston, MA: Artech House Publishers) p 51

[70] Isakov A *et al* 2004 *J. Russ. Laser Res.* **25** 397

Angular distribution of neutrons from high-intensity laser–target interactions

J Davis and G M Petrov

Naval Research Laboratory, Plasma Physics Division, 4555 Overlook Ave SW, Washington, DC 20375, USA

E-mail: jack.davis@nrl.navy.mil and george.petrov@nrl.navy.mil

Abstract

The angular distribution of neutrons formed in nuclear fusion reactions of a high-energy deuteron beam with a deuterated polyethylene (CD_2) was investigated with a Monte Carlo ion beam–target deposition model. The initial conditions were obtained from a two-dimensional particle-in-cell laser–target deposition model. The neutron yield and its angular distribution were studied as a function of peak laser intensity, laser pulse duration and primary target thickness. The proposed scheme for neutron production delivers a typical neutron yield of 10^{-5}–10^{-3} neutrons/ion and 10^5–10^7 neutrons J^{-1} laser energy.

(Some figures in this article are in colour only in the electronic version)

1. Introduction

High-intensity ultrashort pulse lasers are compact and versatile systems that can be employed to induce nuclear fusion reactions. If laser radiation of sufficiently high intensity irradiates a thin planar foil, fast ions with energies in the megaelectronvolt range are generated on the back surface of the foil. These ions can drive nuclear fusion reactions and generate a copious amount of neutrons. Such laser-driven neutron sources are an alternative to the accelerator- and reactor-driven sources offering high brightness, compactness, short duration and relatively low cost. Applications include fast neutron radiography [1], transmutation of nuclear waste [2] and fusion research [3, 4]. Another exciting application, which is currently under intense investigation, is the generation of high brightness neutron beams for neutron activation. Figure 1(a) is a schematic visualization of the neutron activation process. During the first stage, a collimated high-energy ion beam (∼MeV) is generated from the primary target. In the next stage, fast neutrons are born in nuclear fusion reactions driven by the fast ions from a thick (∼1 mm) secondary target made of deuterated material. During the third stage, the neutrons impinge on the target of interest and the interaction of the fast (several megaelectronvolt) neutrons with the target leads to the emission of gamma rays. The gamma-ray 'signature' is unique for each element and, in principle, can be used to identify
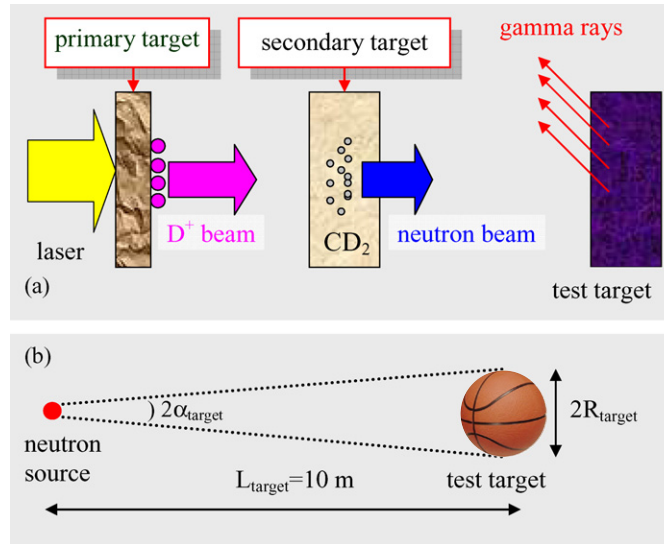
Figure 1. Neutron production concept (*a*) and neutron activation of a distant target (*b*). The laser pulse propagates from left to right along the axis '*x*'.

the constituents of the material producing them. The most challenging aspect of the neutron activation process is to deliver a sufficient number of neutrons on targets located ∼5–50 m from the neutron source (figure 1(*b*)). The problem is that neutrons born in nuclear fusion reactions are scattered (more or less) isotropically and only a tiny fraction of the total number of neutrons will hit a distant target. Thus the problem is not only to produce a large number of neutrons but also to scatter them preferentially in the forward direction. In fact, producing smaller numbers of well collimated neutrons may be advantageous compared with producing a large number of isotropically scattered neutrons for two reasons. First, the number of neutrons on target is determined by the neutron flux and not by the number of neutrons, and second, shielding of personnel and equipment may be alleviated or eliminated. One of the options is to use relatively inexpensive table-top high-intensity lasers, which potentially can generate a collimated beam of neutrons.

Neutron production from high-intensity laser–target interaction has already been demonstrated in a number of experimental [1, 5–17] and theoretical [3, 14–22] studies. The bulk of the work has been done during the last ten years, when ultrashort pulse lasers with parameters suitable for neutron production became available. Most experiments were performed with lasers having energies ranging from a few Joules to about 100 J. The total neutron yield reported is typically 10^4–10^8 neutrons. Due to the differences in laser systems, in particular, delivered laser energy on target, it is better to compare the neutron yield per unit laser energy. Still, the results vary widely: from ∼10^4 neutrons J^{-1} [7,8,12] to ∼10^7 neutrons J^{-1} [5]. A summary of the neutron yield from various experiments is given in table 1. The angular distribution of neutrons is of critical importance for producing a high flux of neutrons. Toupin *et al* studied the angular distribution of neutron emission as a function of laser intensity and maximum electron density [17]. Their results indicate that if the medium generating light ions is highly overdense plasma (such as from laser–thin-foil interaction), the neutrons are emitted preferentially in the forward direction. The neutron production model employed was based on the continuous slowing down approximation of deuterons in a solid target. The deuteron constantly loses energy until its energy drops below a prescribed cut-off value. The neutron

Table 1. Laser and target parameters and neutron yield from high-intensity laser solid interactions.

Target	E (J)	I_0 (W cm^{-2})	T_0 (ps)	Y	Y (n J^{-1})	References
C_8D_8	20	8×10^{18}	1.3	7×10^7 (n sr^{-1})	4×10^7	[5]
CD_2	2	3×10^{19}	0.3	7×10^6 (n)	4×10^6	[6]
CD_2	20	3×10^{18}	0.45	9×10^5 (n)	5×10^4	[7]
CD_2	0.3	2×10^{18}	0.05	1×10^4 (n)	3×10^4	[8]
C_2D_4	0.2	1×10^{18}	0.16	1.4×10^2 (n)	7×10^2	[10]
CD	90	5×10^{19}	0.9–1.2	3×10^6 (n sr^{-1})	4×10^5	[11]
CD_2	5	2×10^{18}	1.5	1×10^5 (n)	2×10^4	[12]
CD	20–50	2×10^{19}	0.45–0.8	1×10^4 (n)	5×10^2	[15]
C_8D_8	2.3	2×10^{19}	0.5	7×10^4 (n sr^{-1})	2×10^4	[16]

yield is calculated via integration of the neutron production differential cross section over the deuteron energy and angular distribution functions. One of the main simplifications of the model is that the deuteron trajectory is a straight line (but as we will see in section 4, this is actually a very good approximation). To overcome this limitation, Habara *et al* [15] and Izumi *et al* [16] used a 3D Monte Carlo code, which tracks the ion trajectory through the secondary target.

Our previous study focused on the first stage of neutron production, i.e. the formation of a high-energy deuteron beam from high-intensity laser–target interactions [23]. The laser–target deposition model of the first stage is a two-dimensional electromagnetic particle-in-cell model. It was employed to study theoretically the production of megaelectronvolt deuterons during the interaction of intense ultrashort laser pulses with a double-layer thin foil. The directionality and energy of the deuteron beam were studied as a function of peak laser intensity, laser pulse duration and target thickness. This paper focuses on the second stage of neutron generation. An ion-beam–target deposition model is developed to calculate the neutron production. The ion transport through a thick deuterated target (CD_2) is simulated using three-dimensional Monte Carlo calculations, as in [15, 16]. Each simulation yields the angular distribution of neutrons and the total neutron yield in absolute units as a result of the nuclear fusion reaction $D + D \rightarrow {}^3He + n$. The model is used to perform a comprehensive parametric theoretical study of the neutron generation, which includes a variation of the peak laser intensity, laser pulse duration and thickness of both layers of the primary target. The neutron yield in absolute units and its angular distribution are presented as a function of these parameters. Section 2 details the ion beam–target deposition model. In section 3 we present the primary and secondary target configurations. A simple model for neutron production with forward directed mono-energetic ions and a more detailed model, which incorporates realistic deuteron energy and angular distributions, are compared in section 4. In this section we also perform a parametric study of the angular flux of neutrons, and summarize our findings in section 5.

2. Ion beam–target deposition model

2.1. Monte Carlo simulations

We start this section by briefly describing the output of the laser–target deposition model in order to explain how it transitions to the ion beam–target deposition model described below. For given laser and primary target parameters at the end of the simulation the deuteron energy and angle with respect to the target normal (the $+x$ direction) are recorded and stored in a file. Both parameters are known from the particle movement module of the electromagnetic model. These data serve as input of the ion beam–target deposition model.

The ion beam–target deposition model closely follows the neutron production models developed by Habara *et al* [15], Izumi *et al* [16] and Toupin *et al* [17]. In essence, this is a 3D Monte Carlo code, which follows the transport of ions through the secondary target. Ions are launched one by one from the surface of the secondary target with a given energy E_i^{inc} and angle θ_i^{inc} with respect to the normal surface. The information for each ion comes from the output file of the laser–target deposition model, as described in the previous paragraph. The ion transport through the secondary target is based upon the following assumptions:

- The secondary target is sufficiently thick (a few millimeters) so that even the most energetic deuterons are completely stopped inside. Its normal points in $+x$, the direction of laser propagation.
- The ion distribution is axisymmetric with respect to the laser propagation direction.
- The neutron distribution is also axisymmetric with respect to the same axis.
- The ion transport is based on the continuous slowing down approximation using the concept of stopping power and angular scattering via small-angle scattering in collisions with the atoms of the secondary target. The stopping power depends on the incident ion energy, target material and target density.

The ion transport through the secondary target is modeled by following the ion energy and trajectory in space according to the following algorithm. The ion is assigned initial spatial coordinates $\vec{r}_i = (0, 0, 0)$, energy $E_i = E_i^{\text{inc}}$ and a velocity vector defined by a polar angle $\theta_i = \theta_i^{\text{inc}}$ with respect to the normal surface and an azimuthal angle φ_i chosen randomly in the interval $[0-2\pi]$. The ion advances in steps traversing a distance Δl, which is chosen according to the initial ion energy so that the deuteron makes a sufficient number of steps ($\sim 10^3$ or more) until it stops. The magnitude of the energy loss per step

$$\Delta E_i = S(E_i)\Delta l \tag{1}$$

is determined by the stopping power $S(E_i)$. The deuteron is then moved to a new position $\vec{r}_i \to \vec{r}_i + \Delta \vec{r}_i$, $\Delta \vec{r}_i = (\Delta l \sin\theta_i \cos\varphi_i, \Delta l \sin\theta_i \sin\varphi_i, \Delta l \cos\theta_i)$, where it experiences a pseudo-scattering and changes direction by selecting new azimuthal and polar angles. The azimuthal angle φ_i^{cm} in the center-of-mass system is chosen randomly in the interval $[0-2\pi]$. The polar angle θ_i^{cm} in the same system is sampled from the multiple-scattering distribution function for the projected angle of scattering

$$P(\theta) = \frac{1}{\sqrt{\pi \langle\theta^2\rangle}} \exp\left(-\frac{\theta^2}{\langle\theta^2\rangle}\right), \tag{2}$$

which is appropriate for describing multiple small-angle scattering of high-energy ions in collisions with the target atoms of the secondary target. A deuteron traversing a distance Δl is scattered at an angle whose mean square $\langle\theta^2\rangle$ is given by the well-known Jackson's formula [24]

$$\langle\theta^2\rangle = 4\pi N_t \left(\frac{4Z_t e^2}{4\pi \varepsilon_0 E_i}\right)^2 \ln(204 Z_t^{-1/3})\Delta l, \tag{3}$$

where N_t and Z_t are the secondary target density and charge number, respectively (e is the electron charge and ε_0 is the permittivity of free space). The conversion of the post-collision direction of the deuteron $\Omega^{\text{cm}} = \{\theta_i^{\text{cm}}, \varphi_i^{\text{cm}}\}$ from the center-of-mass system to the laboratory system $\Omega^L = \{\theta_i, \varphi_i\}$ determines the new deuteron direction in the laboratory system after the pseudo-collision takes place [25]. The above algorithm is applied at each step until the ion energy becomes less than the cut-off energy $E_i^{\text{cut-off}}$ (~ 1 KeV).
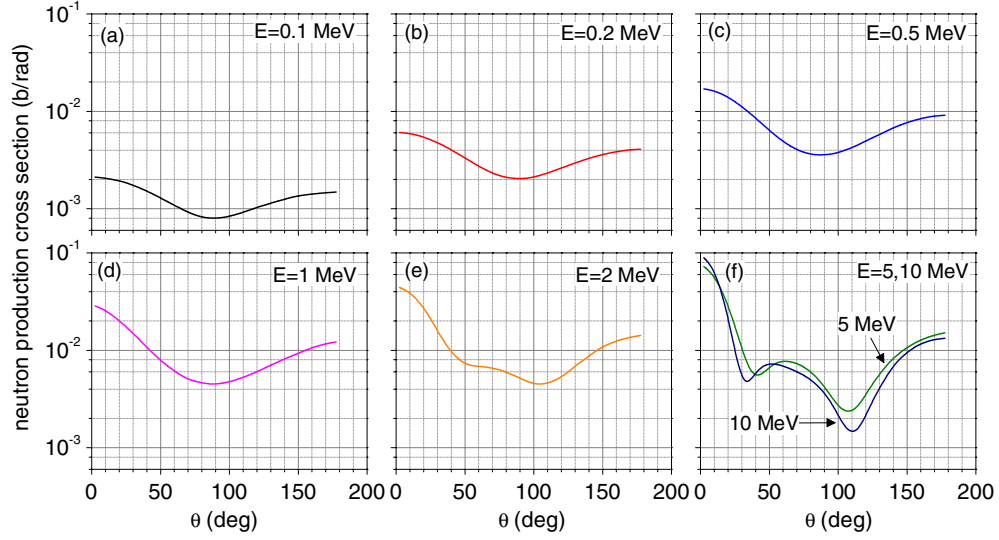
4

Figure 2. Differential cross section for neutron production $d\sigma(E_i, \theta_n)/d\Omega_n$ for deuteron energies E_i of 0.1 MeV (*a*), 0.2 MeV (*b*), 0.5 MeV (*c*), 1 MeV (*d*), 2 MeV (*e*) and 5 and 10 MeV (*f*). Data from [26].

During each step the neutron flux to specific directions of observation is also calculated. The increment of the neutron flux at polar angle α_n into the solid angle $d\Omega_n$ for deuteron traversing a distance Δl is calculated according to

$$\Delta\left(\frac{dY_n(\alpha_n)}{d\Omega_n}\right) = \frac{d\sigma(E_i, \theta_n)}{d\Omega_n}n_D\Delta l, \qquad (4)$$

where n_D is the density of deuterium substance in the secondary target (a value provided in section 3) and $d\sigma(E_i, \theta_n)/d\Omega_n$ is the differential cross section for neutron production[1] [26], plotted in figure 2. It is important to note that the neutron production direction θ_n in equation (4) is accounted for in a coordinate system with axis pointing in the direction of the deuteron velocity, which is rotated with respect to the laboratory coordinate system. In other words, θ_n is measured with respect to θ_i, while the polar angles α_n and θ_i are measured (in the laboratory system) with respect to the secondary target normal. A transformation of the directional vector from the rotated coordinate systems to that of the laboratory system yields $\theta_n = \cos^{-1}(\cos\theta_i\cos\alpha_n + \sin\theta_i\sin\alpha_n\cos\varphi_i)$, which directly relates angle α_n to θ_n via the ion directional angles $\{\theta_i, \varphi_i\}$ [17].

2.2. Simple model: mono-energetic deuteron beam normally incident on a target

It is fairly straightforward to calculate the neutron yield in the special case when the deuterons are mono-energetic, normally incident upon the secondary target and move in a straight line inside the secondary target until they stop. The neutron yield at an angle $\theta_n \equiv \alpha_n \ (0 \leqslant \theta_n \leqslant \pi)$ relative to the direction of the deuteron beam is calculated by integrating the ratio of the nuclear

---

[1] The cross section is tabulated only for incident deuteron energies below 13.8 MeV. For $E_i > 13.8$ MeV we scaled the magnitude of the total cross section and assumed the same angular distribution as that for the largest tabulated energy available (13.8 MeV).

fusion differential cross section to the stopping power from the initial deuteron energy E_i^{inc} to the final cut-off energy $E_i^{\text{cut-off}}$ [6, 17]:

$$\frac{\mathrm{d}Y(E_i^{\text{inc}}, \theta_n)}{\mathrm{d}\Omega} = \int_{E_i^{\text{cut-off}}}^{E_i^{\text{inc}}} \frac{1}{S(E)} \frac{\mathrm{d}\sigma}{\mathrm{d}\Omega}(E, \theta_n)\, \mathrm{d}E. \tag{5}$$

Formula (5) is the number of neutrons per steradian per incident ion. In spite of the simplifications involved, formula (5) is very useful. The neutron yield can be tabulated for a set of incident ion energies E_i^{inc} and neutron direction angles θ_n. Further integration over the ion energy distribution yields the total neutron production, as was done in [17].

3. Primary and secondary target parameters

The primary target is a two-layer thin foil with thickness between 0.1 and $1\,\mu$m. The front layer is made of high-Z material. The rear layer is very thin (0.01–0.1 μm) and is made of deuterium-containing material. The choice of high-Z–low-Z material is motivated by the observation that if the ratio of mass to charge for the front and rear material is sufficiently large, the light ions from the rear surface are accelerated much more efficiently than the heavy ones. The front layer material is gold, a common substance in this kind of high-intensity laser–target interactions. The plasma slab corresponding to this layer has a thickness L_{Au}, density n_{Au} and charge $Z_{\text{Au}} - 1$, respectively. For simplicity we assumed that the rear layer is made of pure deuterium with thickness and density L_D and n_D, respectively. Both the front and the rear layers have the form of a disc with a prescribed diameter D_{Au} and D_D, respectively.

The secondary target is a thick slab of deuterated material. We chose deuterated polyethylene (CD_2), which is commonly used in both experiments and simulations. The density of CD_2 ($1.105 \times 10^3\,\text{kg m}^{-3}$) [27] determines the fractional densities of carbon and deuterium in the target: $n_C'' = 4.1 \times 10^{28}\,\text{m}^{-3}$ and $n_D'' = 8.2 \times 10^{28}\,\text{m}^{-3}$, respectively. The material and its density, in turn, determine the stopping power of deuterons in the secondary target. Since the stopping power depends on the projectile velocity, the stopping power of D^+ in carbon and deuterium is computed by shifting the corresponding stopping power for H^+ in the energy domain, i.e. $S_1^{D^+-X}(E) = S_1^{H^+-X}(E/2)$, where $X = C, D$ stands for carbon and deuterium [28, 29]. The computed individual stopping powers per atom $S_1^{D^+-C}(E)$ and $S_1^{D^+-D}(E)$ are shown in figure 3(a) and the total stopping power of D^+ in CD_2 $S^{D^+-CD_2}(E) = S_1^{D^+-C}(E)n_C'' + S_1^{D^+-D}(E)n_D''$ is shown in figure 3(b). The latter is the stopping power in the right-hand side of equation (1).

4. Results and discussions

4.1. Neutron yield from a mono-energetic deuteron beam normally incident on a target

We commence with the simplest case of a mono-energetic beam of deuterons normally incident upon the secondary target (section 2.2). We performed a series of simulations by launching deuterons with energies $E_i^{\text{inc}} = 0.1, 0.3, 1, 3, 10$ and $30\,\text{MeV}$ at incident angle normal to the surface. The angular distribution of the neutron yield per deuteron for various incident deuteron energies is shown in figure 4 (solid lines). It can be separated into two regions, depending on the incident ion energy: for deuteron energy below about 1 MeV the angular distribution is close to uniform, while for higher energies it is peaked forward. The total neutron yield (integrated over the scattering angle), together with the total cross section for neutron production, is plotted in figure 5. The total neutron yield increases nonlinearly with
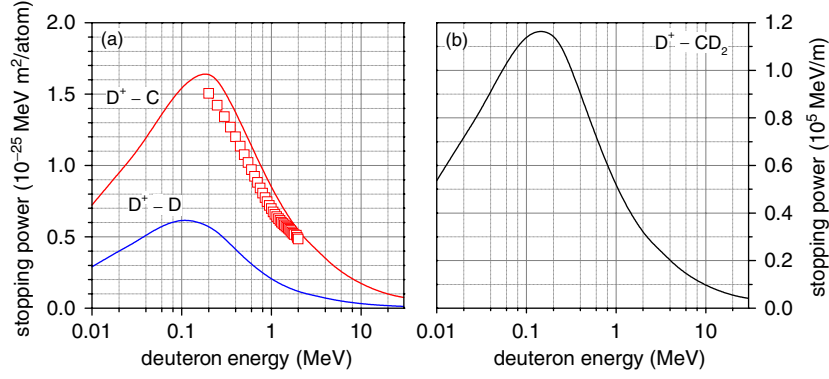
Figure 3. Stopping power per atom of D^+ in C and D (*a*) and total stopping power of D^+ in CD_2 (*b*) versus deuteron energy. Symbols: stopping power per atom of D^+ in C [34].
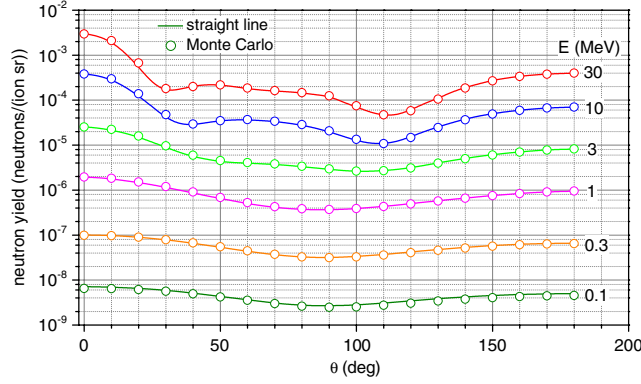

Figure 4. Angular distribution of the neutron yield per ion $dY(E_i^{inc}, \theta_n)/d\Omega$ versus scattering angle for various incident deuteron energies. Simple model—solid lines, symbols—Monte Carlo model.

the deuteron energy and can be well approximated as

$$
Y(E_i^{inc}) = \begin{cases} 7.8 \times 10^{-6}(E_i^{inc})^{1.7} & E_i^{inc} \geqslant 1\,\text{MeV}, \\ 7.8 \times 10^{-6}(E_i^{inc})^{2.2} & E_i^{inc} \leqslant 1\,\text{MeV}. \end{cases}
$$

The near-quadratic dependence of the neutron yield versus incident deuteron energy suggests that in simulations with deuterons having sufficient energy spread the high-energy deuterons from the tail of the ion energy distribution function (IEDF) may contribute significantly to the total neutron yield. This point is proven in the following sub-section.

Our next task is to study the impact of scattering on the neutron yield. We performed another series of simulations by launching mono-energetic ions with the same incident energy and angle. The only difference from the previous set of simulations is that now the deuteron trajectory is modeled with Monte Carlo, rather than being a straight line. For improved statistics, the neutron yield is averaged over $\sim 10^3$ ions (for each incident ion energy). The angular distribution of the neutron yield per ion is plotted in figure 4 (symbols). The results show that the actual deuteron trajectory is of little importance for the neutron yield. This is confirmed in figure 6, where sample deuteron trajectories are plotted for the same incident deuteron energies. The abscissa is the deuteron position in the direction parallel to the angle
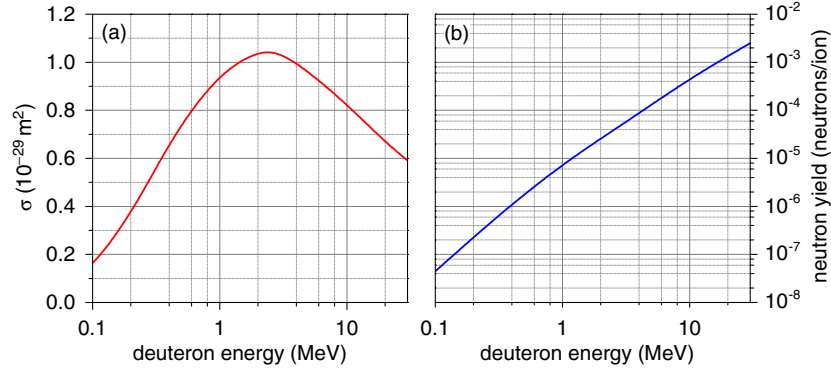
Figure 5. Total cross section for neutron production $\sigma(E_i) = \int_{\Omega_n}(d\sigma(E_i, \theta_n)/d\Omega_n)\,d\Omega_n$ (*a*) and total neutron yield $Y(E_i^{inc}) = \int_{\Omega_n}(dY(E_i^{inc}, \theta_n)/d\Omega_n)d\Omega_n$ versus deuteron energy (*b*).
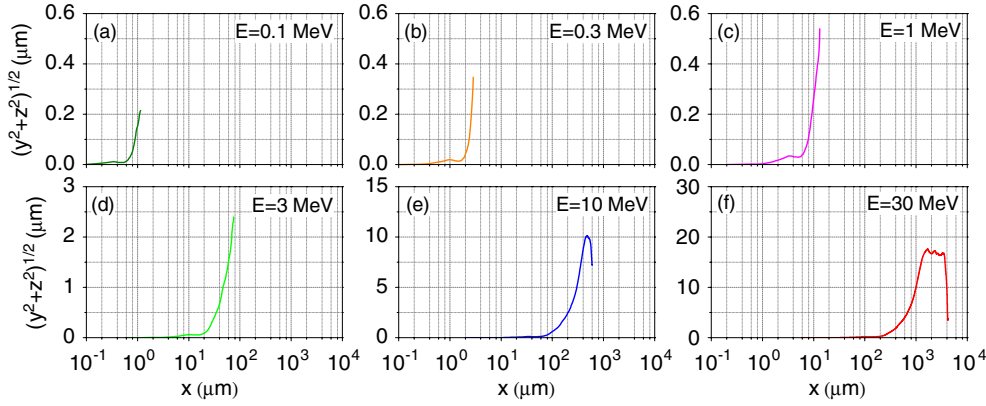

Figure 6. Deflection in the transverse direction $\sqrt{y^2 + z^2}$ versus longitudinal position of deuteron trajectories for incident deuteron energies 0.1 MeV (*a*), 0.3 MeV (*b*), 1 MeV (*c*), 3 MeV (*d*), 10 MeV (*e*) and 30 MeV (*f*).

of incidence (laser propagation direction $+x$), while the ordinate plots the deflection $\sqrt{y^2 + z^2}$ in the transverse direction. The transverse deflection at the end of the deuteron trajectory is very small compared with the penetration depth and only after the deuteron has lost most of its initial energy. Since the bulk of the neutron production occurs at high deuteron energy, the last segment of the deuteron trajectory has negligible contribution to the total neutron yield. These results confirm that if the deuteron trajectory is assumed to be a straight line, the neutron production is accurately computed in this regime of laser–target interactions.

4.2. Parametric study: variation of the peak laser intensity, laser pulse duration and primary target thickness

In this sub-section a parametric study of the angular distribution of neutrons and neutron yield (in absolute units) is performed. Both are calculated as a function of peak laser intensity, laser pulse duration and target thickness. The laser and primary target parameters are varied in a range suitable for neutron generation: peak laser intensity 10^{23}–10^{25} W m^{-2} (10^{19}–10^{21} W cm^{-2}), deuterium layer thickness 0.01–0.1 μm and gold layer thickness 0.1–1 μm. The laser radiation is an ultrashort pulse of linearly polarized light normally
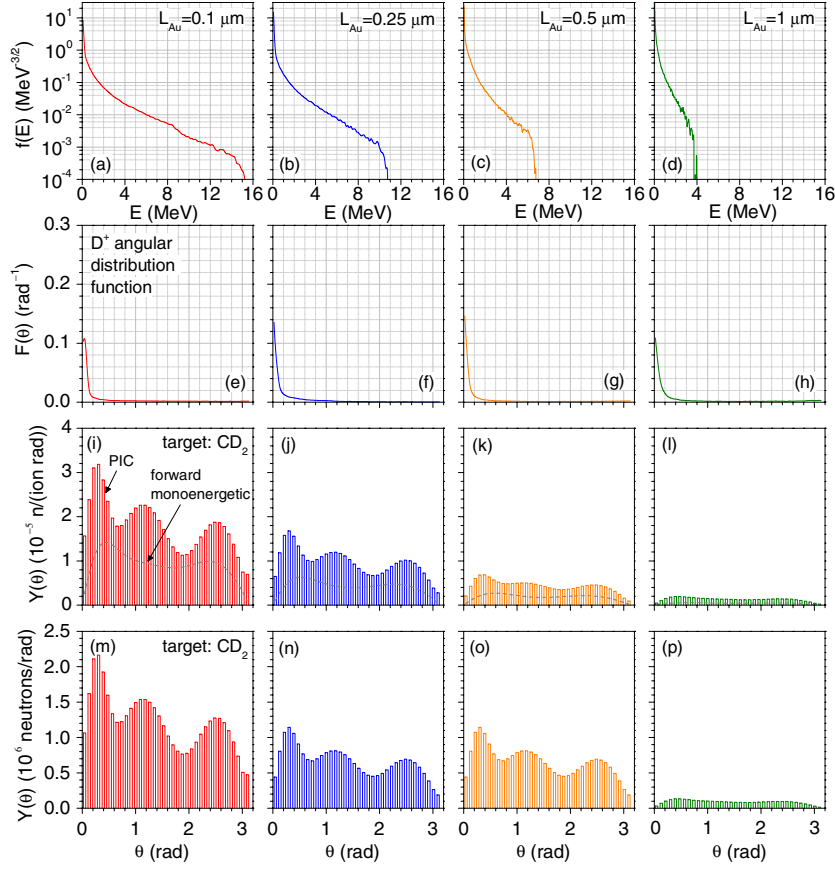
Figure 7. Deuteron energy distribution function (a)–(d), angular distribution function (e)–(h), neutron yield per ion versus scattering angle (i)–(l) and total neutron yield versus scattering angle (m)–(p) for different thicknesses L_{Au} of the Au layer. The laser and target parameters are $I_0 = 10^{24}\,\mathrm{W\,m^{-2}}$, $\lambda_0 = 1\,\mu\mathrm{m}$, $R_0 = 3\,\mu\mathrm{m}$, $\tau_0 = 80\,\mathrm{fs}$, $E_{laser} = 1.13\,\mathrm{J}$, $L_D = 0.05\,\mu\mathrm{m}$, $n_e \cong 100 n_c$.

incident on the target, propagating in the $+x$ direction. The laser pulse has a spatio-temporal profile $I(y, t) = I_0 \sin^2(\pi t/\tau_0) \exp(-(y/R_0)^2)$ with I_0 being the peak laser intensity, τ_0 the laser pulse duration and R_0 the laser spot radius. Details of the simulation parameters are given in [23].

The angular distribution of the neutron yield per ion and the total neutron yield for different thicknesses of the Au layer is shown in figure 7. The deuteron angular and energy distribution function, which have been analyzed in [23], are shown for reference. The laser and target parameters are peak laser intensity $I_0 = 10^{24}\,\mathrm{W\,m^{-2}}$, laser wavelength $\lambda_0 = 1\,\mu\mathrm{m}$, laser spot size $R_0 = 3\,\mu\mathrm{m}$, laser pulse duration $\tau_0 = 80\,\mathrm{fs}$ ($\tau_{FWHM} \equiv \tau_0/2 = 40\,\mathrm{fs}$), input laser energy $E_{laser} = \pi R_0^2 I_0 \tau_{FWHM} = 1.13\,\mathrm{J}$ and deuterium layer thickness $L_D = 0.05\,\mu\mathrm{m}$. The primary target is an overdense plasma with $n_e \cong 100 n_c$. The angular distribution of neutrons is computed in elementary angular bins $\alpha_n = (n + 1/2)\Delta\alpha_n, n = 0, \ldots, 35$. The width of each angular bin is $\Delta\alpha_n = \pi/36 = 8.73 \times 10^{-2}\,\mathrm{rad}$ (corresponding to $5°$). The neutron yield (the average number of neutrons per ion per radian) to the directions of observation α_n

$$Y_n(\alpha_n) = 2\pi \sin(\alpha_n) \frac{dY_n(\alpha_n)}{d\Omega_n} \tag{6}$$

is plotted in figures 7(*i*)–(*l*). The dashed line refers to the simplistic model from the previous sub-section (mono-energetic deuteron beam with incident energy equal to the mean deuteron energy and normally incident on the target). The Monte Carlo calculations differ from the simplistic ones in two respects: the IEDF (mono-energetic versus actual) and the ion angular distribution function (normal incidence angle versus actual angle of incidence). The latter plays a minor role as the deuteron beam is only slightly divergent, as seen in the second row of figures. The major difference is expected to be the impact of the IEDF. As discussed in the previous sub-section, the neutron yield increases nonlinearly with the deuteron energy. In addition, the IEDF has a very long tail with maximum (cut-off) deuteron energy ∼10 times the mean deuteron energy (figure 7, first row of figures). The third row of figures provides a direct comparison between the simplistic and actual cases. The simplified version of neutron production underestimates the actual neutron yield by a factor of two. Not surprisingly, the angular distribution of the neutron yield in both cases is similar, since most of the ions have a very small angle of incidence (with respect to the target normal). The total neutron yield (last row of figures) is equal to the neutron yield per deuteron multiplied by the total number of deuterons $N_{D^+} = \pi R_0^2 L_D n_D = 6.8 \times 10^{10}$ in the rear layer of the primary target. With the gold layer thickness increasing the neutron yield decreases. This can be expected since both the mean deuteron energy decreases with the gold layer thickness increasing and the high-energy tail of IEDF becomes depleted.

The neutron yield versus variation of the thickness of the deuterium layer of the primary target is more subtle. The thinner deuterium layer favors the production of higher energy deuterons (figure 8, first row) with narrower angular distribution (figure 8, second row). With an increase in the deuterium layer thickness the neutron yield per ion declines (figure 8, third row); however, the number of deuterons, which scales as $N_{D^+} \sim L_D$, increases and so does the total neutron yield. The trade-off leads to a broad peak with an optimum thickness of the deuterium layer between 50 and 100 nm. According to figure 8 the neutron yield is insensitive with respect to the deuterium layer thickness.

The next sequence of figures illustrates the neutron yield versus the input laser parameters. The deuteron energy and angular distribution function for four peak laser intensities varying from $I_0 = 10^{23}\,\mathrm{W\,m^{-2}}$ to $I_0 = 10^{25}\,\mathrm{W\,m^{-2}}$ are plotted in figure 9. We first make a comparison of the simplistic model with the Monte Carlo simulations in order to explore the role of the IEDF on the neutron production. At peak laser intensity of $I_0 \sim 10^{23}\,\mathrm{W\,m^{-2}}$ the neutron yield from the Monte Carlo code is much higher compared with that of the simplistic model, while at peak laser intensity of $I_0 \sim 10^{25}\,\mathrm{W\,m^{-2}}$ the exact opposite is observed: both models yield essentially the same result. This behavior can be explained by comparing the IEDFs for both intensities. For the higher peak laser intensity $I_0 \sim 10^{25}\,\mathrm{W\,m^{-2}}$ the ions form a beam with a relatively broad energy spectrum (figure 9(*d*)), which is in contrast to the two-temperature Maxwellian IEDF at the lower peak intensity (figures 9(*a*)–(*c*)). The comparison clearly shows the role of the IEDF on the neutron yield. The most remarkable feature of the angular distribution of the neutron yield is the location of the most favorable direction for neutron production. At low laser intensity it has an angular dependence close to a *sine* function, peaking around 60–120°, indicative of uniform distribution in space (figures 9(*m*)–(*n*)), but with an increase in the peak laser intensity the peak shifts to smaller angles (figure 9(*o*)) and for the highest laser intensity it peaks in the direction of laser propagation (figure 9(*p*)). The increase in the laser pulse duration has an impact similar to that of increasing the peak laser intensity. Both the neutron yield increase and the angular distribution become more forward directed with the laser pulse duration increasing (figure 10).

A summary is given in figure 11, where the average incident deuteron energy $\langle E_i^{\mathrm{inc}} \rangle$, average penetration depth, the total neutron yield per ion, the number of deuteron ions and the
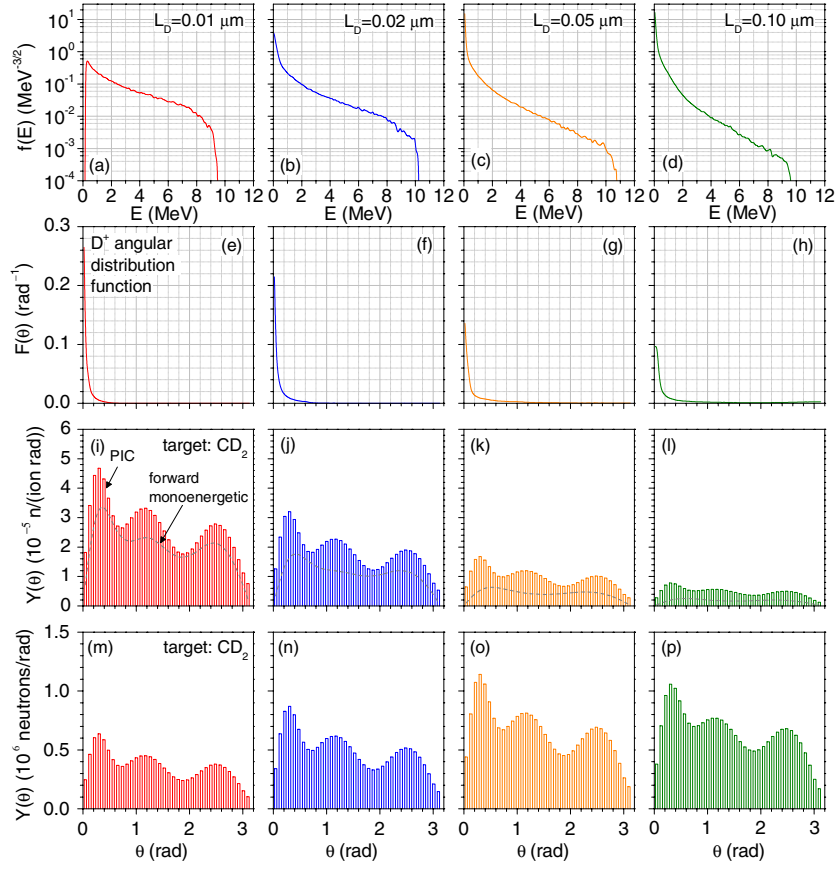
Figure 8. Deuteron energy distribution function (a)–(d), angular distribution function (e)–(h), neutron yield per ion versus scattering angle (i)–(l) and total neutron yield versus scattering angle (m)–(p) for different thicknesses L_D of the D layer. The laser and target parameters are $I_0 = 10^{24}\,\mathrm{W\,m^{-2}}$, $\lambda_0 = 1\,\mu\mathrm{m}$, $R_0 = 3\,\mu\mathrm{m}$, $\tau_0 = 80\,\mathrm{fs}$, $E_{\mathrm{laser}} = 1.13\,\mathrm{J}$, $L_{\mathrm{Au}} = 0.25\,\mu\mathrm{m}$, $n_e \cong 100 n_c$.

total neutron yield are plotted versus thickness of the gold and deuterium layers, peak laser intensity and laser pulse duration. For the intermediate peak laser intensity of $I_0 = 10^{24}\,\mathrm{W\,m^{-2}}$ the neutron yield is 10^5–10^7 neutrons, depending on the laser pulse duration. Our simulations are in close agreement with the simulations in [17], which report neutron yield of 1.4×10^6 at comparable conditions (peak laser intensity, laser wavelength, spot size and plasma density). The most noteworthy characteristics regarding the total neutron yield is the sharp increase in magnitude with the peak laser intensity (figure 11(s)). This result is in agreement with the simulations performed by Toupin *et al* [17], who observed an increase in the neutron yield of four orders of magnitude when the peak laser intensity increases from $I_0 = 10^{23}\,\mathrm{W\,m^{-2}}$ to $I_0 = 2 \times 10^{24}\,\mathrm{W\,m^{-2}}$ (cf figure 11(s)). Measurements of the neutron yield in the same interval of peak laser intensities show a similar trend [6].

The parametric study demonstrates a direct correlation between the neutron yield and directionality and the ion beam characteristics. The latter are determined by various input parameters (laser and target), which can be controlled, but they are also subject to 'external factors', not accounted for in the present model. One of them is the 2D Cartesian geometry in the laser–target deposition model. We use only three EM field components (E_x, E_y and B_z), while
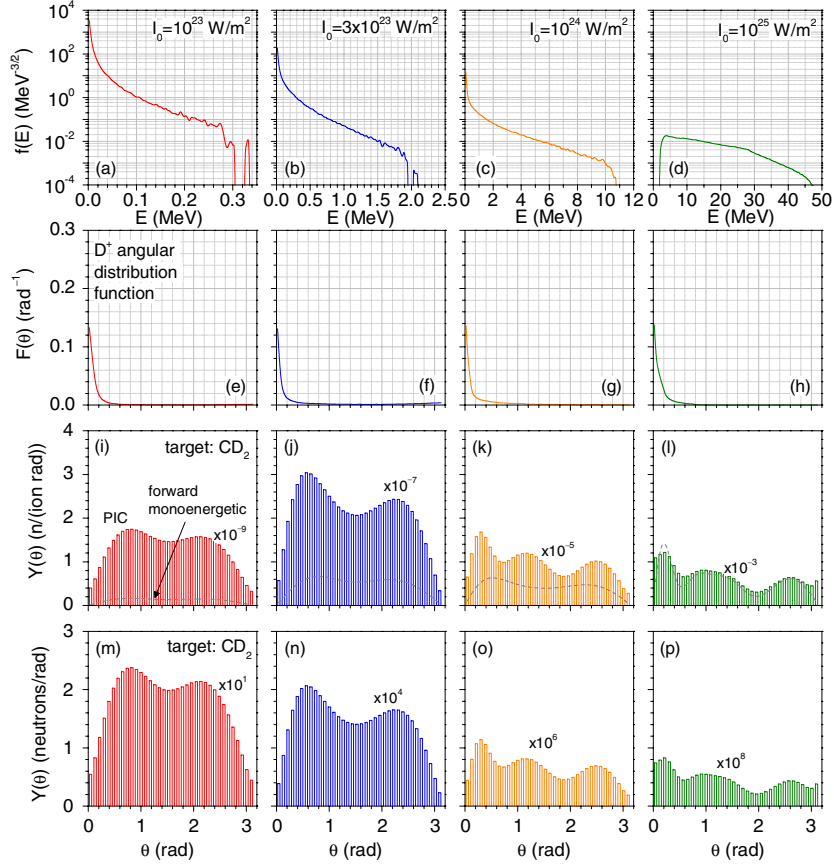
Figure 9. Deuteron energy distribution function (a)–(d), angular distribution function (e)–(h), neutron yield per ion versus scattering angle (i)–(l) and total neutron yield versus scattering angle (m)–(p) for different peak laser intensities I_0. The laser and target parameters are $\lambda_0 = 1\,\mu$m, $R_0 = 3\,\mu$m, $\tau_0 = 80$ fs, $L_{Au} = 0.25\,\mu$m, $L_D = 0.05\,\mu$m, $n_e \cong 100 n_c$.

a truly 3D electromagnetic model follows all six components. Thus three-dimensional effects, such as current filamentation and quasistatic magnetic field generation [30, 31], and angular distributions of the accelerated electrons [32] are not fully accounted for. For example, a strong self-generated longitudinal magnetic field has been observed in simulations [31], which would confine the electrons and ions and reduce the divergence of the deuteron beam. Another simplification is the neglect of collisions, though it is still a reasonable approximation at the laser intensities and particle kinetic energies (∼MeV) we deal with. Since the deuterons already form a fairly collimated beam, none of the above simplifications is expected to affect the final results on neutron generation.

4.3. Neutron spectra

There are a variety of applications for the spectrum of energetic neutrons ranging from nuclear cross section information, neutron imaging, fusion and fusion reactions and the material reactions that produce gamma radiation. Both neutrons and neutron activated gamma radiation are finding widespread application in the detection of explosive and nuclear materials. A useful
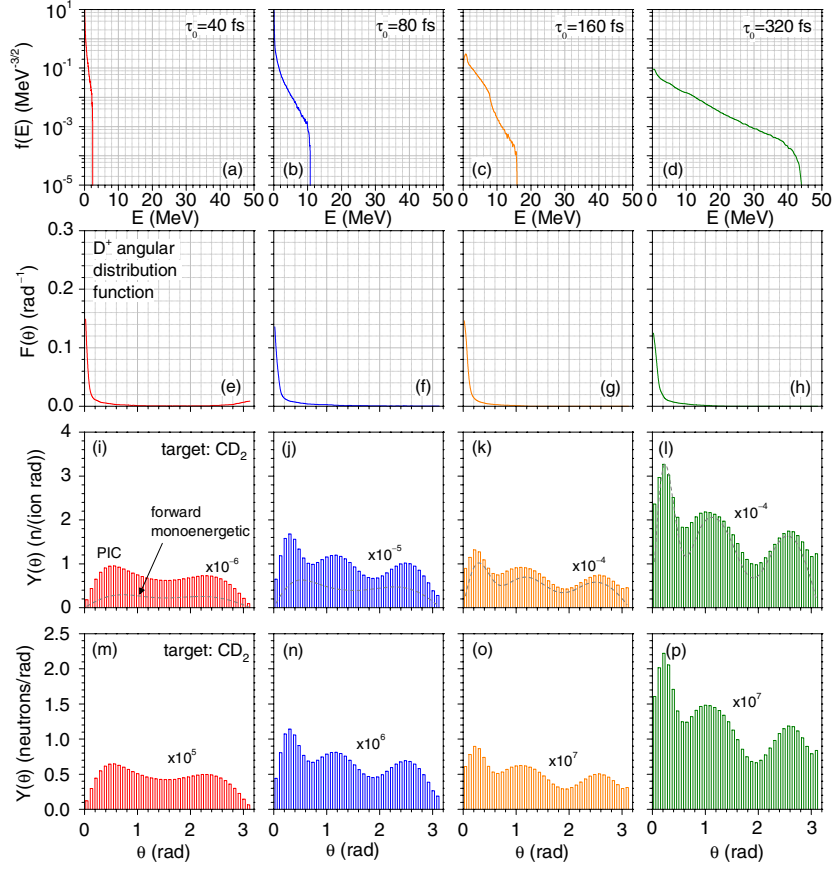
Figure 10. Deuteron energy distribution function (a)–(d), angular distribution function (e)–(h), neutron yield per ion versus scattering angle (i)–(l) and total neutron yield versus scattering angle (m)–(p) for different laser pulse durations τ_0. The laser and target parameters are $I_0 = 10^{24}$ W m^{-2}, $\lambda_0 = 1\,\mu$m, $R_0 = 3\,\mu$m, $L_{Au} = 0.25\,\mu$m, $L_D = 0.05\,\mu$m, $n_e \cong 100 n_c$.

discussion can be found in the paper by Ledingham *et al* [33]. Figure 12 shows integrated neutron spectra for peak laser intensities $I_0 = 10^{23}$, 10^{24} and 10^{25} W m^{-2}. Neutrons are emitted with energies

$$E_n = \left(\sqrt{2 + 19.6/E_i \,(\text{MeV}) + \cos^2 \theta_n} + \cos \theta_n \right)^2 E_i/8, \qquad (7)$$

which depend on the incident deuteron energy [17]. At low E_i^{inc} the neutron energy is not sensitive with respect to the incident deuteron energy and peaks near 2.45 MeV, while for high E_i^{inc} the neutron is emitted with energy comparable to that of the incident deuteron. For the lowest laser intensity the neutron spectrum is centered around 2.45 MeV. This is because the deuteron incident energies are well below 1 MeV. For the intermediate intensity the deuteron energies extend to ~10 MeV, showing a double peak at around 2 and 3.5 MeV. For the highest peak laser intensity of $I_0 = 10^{25}$ W m^{-2} the ions have incident energies between 2 and 50 MeV, resulting in a neutron spectrum peaked at around 2.5 MeV with a long tail extending to tens of megaelectronvolts. These high-energy neutrons can be more efficient for neutron activation.
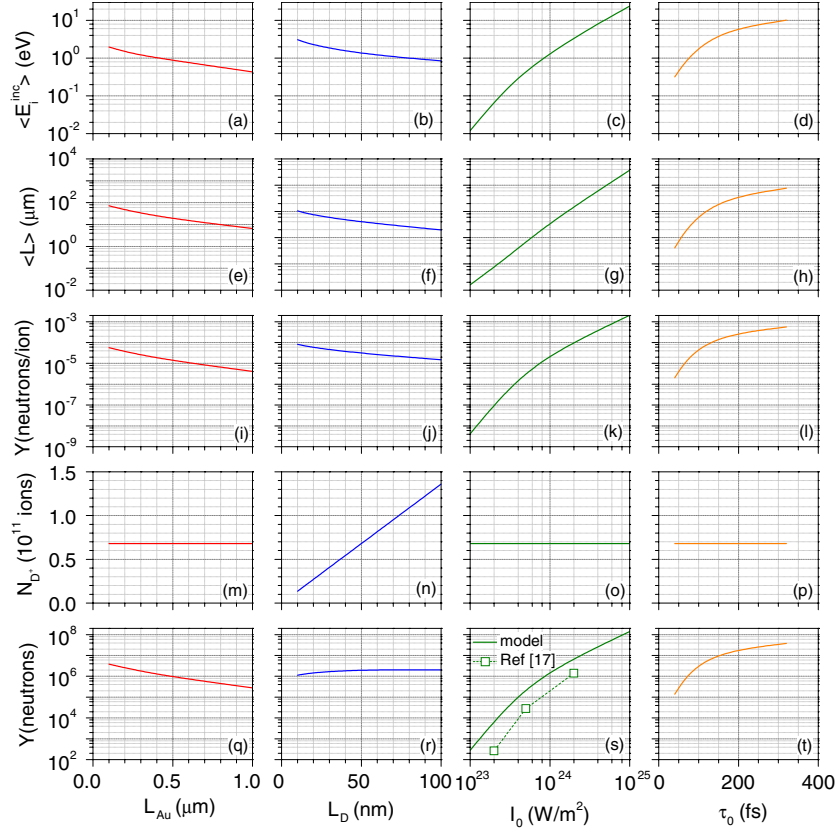
Figure 11. Average incident deuteron energy (a)–(d); average penetration depth of deuterons in the secondary target (e)–(h) neutron yield per ion (i)–(l), total number of deuterons $N_{D^+} = \pi R_0^2 L_D n_D$ (m)–(p) and total neutron yield (q)–(t) for different Au layer thickness (first column) D layer thickness (second column), peak laser intensity (third column) and laser pulse duration (right column). Symbols—simulations by Toupin *et al* [17].
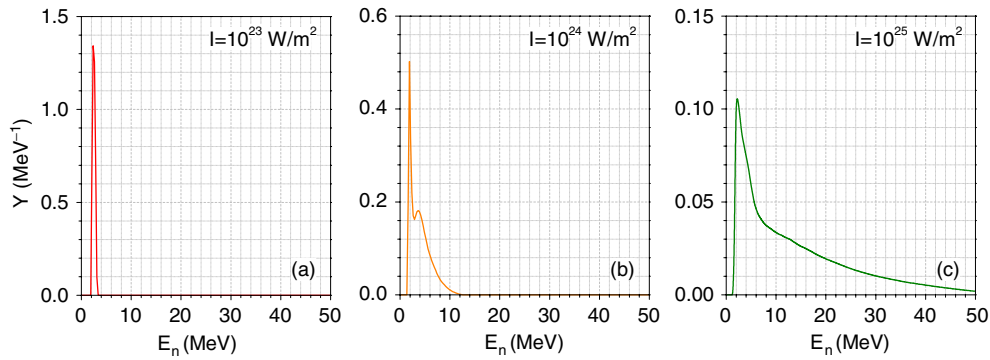

Figure 12. Neutron spectrum for peak laser intensities $I_0 = 10^{23}$ (a), 10^{24} (b) and 10^{25} W m^{-2} (c). Laser and target parameters: $\lambda_0 = 1\,\mu$m, $R_0 = 3\,\mu$m, $\tau_0 = 80$ fs, $L_{Au} = 0.25\,\mu$m, $L_D = 0.05\,\mu$m, $n_e \cong 100 n_c$.

4.4. Neutron activation

Our final goal is to estimate the number of neutrons hitting the test target. Due to the wide variety of targets (particularly size) and distance to target, we will limit the study to one typical case. We selected a target the size of a basketball (radius $R_{\text{target}} = 0.12 \, \text{m}$) located $L_{\text{target}} = 10 \, \text{m}$ away from the neutron source (figure 1(*b*)). For typical laser and primary target parameters ($I_0 = 10^{24} \, \text{W m}^{-2}$, $\lambda_0 = 1 \, \mu\text{m}$, $R_0 = 3 \, \mu\text{m}$, $\tau_0 = 80 \, \text{fs}$, $E_{\text{laser}} = 1.13 \, \text{J}$, $L_{\text{Au}} = 0.25 \, \mu\text{m}$ and $L_{\text{D}} = 0.05 \, \mu\text{m}$) the number of neutrons on the test target is approximately

$$Y_{\text{target}} \approx \alpha_{\text{target}} Y_0, \tag{8}$$

where $\alpha_{\text{target}} = R_{\text{target}}/L_{\text{target}} = 0.012 \, \text{rad}$ ($\sim 0.7°$) is the half-angle from which the target is visible from the neutron source. Inserting the value of the neutron yield in the first angular bin $Y_0 = 4.4 \times 10^5$ neutrons rad^{-1} (figure 7(*o*)), we get $Y_{\text{target}} \approx 5 \times 10^3$ neutrons.

5. Conclusion

Numerical simulations of the angular distribution of neutrons from high-intensity laser–thin-foil interaction using a 3D Monte Carlo code are presented. The study covers variations of target thickness, peak laser intensity and laser pulse duration of the primary target. The neutron yield per ion and the total neutron yield are calculated as a function of these parameters. The results are compared with a simple model of neutron production from a mono-energetic deuteron beam normally incident on a target. Our findings can be summarized as follows:

 (i) With increasing peak laser intensity or laser pulse duration the magnitude of the neutron yield increases nonlinearly. The neutron yield decreases with the thickness of the gold layer increasing and it is insensitive to the thickness of the deuterium layer of the primary target.
 (ii) The angular distribution of neutrons shows a weak dependence on the target thickness, but the forward scattering improves significantly with increasing either the peak laser intensity or the laser pulse duration. The optimum conditions for forward neutron scattering are a thin primary target (gold layer thickness $L_{\text{Au}} = 0.1$–$0.5 \, \mu\text{m}$, deuterium layer thickness $L_{\text{D}} = 0.01$–$0.1 \, \mu\text{m}$) and laser intensity $I_0 > 10^{24} \, \text{W m}^{-2}$.
 (ii) The typical neutron yield is 10^{-5}–10^{-3} neutrons/ion and 10^5–10^7 neutrons J^{-1} laser energy.
 (iii) The simulation results show that for a typical arrangement of laser and target parameters some $\sim 10^4$ neutrons can be put on a target $\sim 10 \, \text{m}$ away.

Acknowledgments

References

[1] Lancaster K L *et al* 2004 *Phys. Plasmas* **11** 3404
[2] Magill J, Galy J and Zagar T 2006 *Lect. Notes Phys.* **694** 131
[3] Perkins L J, Logan B G, Rosen M D, Perry M D, Diaz de la Rubia T, Ghoniem N M, Ditmire T, Springer P T and Wilks S C 2000 *Nucl. Fusion* **40** 1
[4] Habara H, Norreys P A, Kodama R, Stoeckl C and Glebov V Yu 2006 *Fusion Sci. Technol.* **49** 517
[5] Norreys P A, Fews A P, Beg F N, Bell A R, Dangor A E, Lee P, Nelson M B, Schmidt H, Tatarakis M and Cable M D 1998 *Plasma Phys. Control. Fusion* **40** 175

[6] Disdier L, Garconnet J-P, Malka G and Miquel J-L 1999 *Phys. Rev. Lett.* **82** 1454
[7] Youssef A, Kodama R, Habara H, Tanaka K A, Sentoku Y, Tampo M and Toyama Y 2005 *Phys. Plasmas* **12** 110703
[8] Hilscher D, Berndt O, Enke M, Jahnke U, Nickles P V, Ruhl H and Sandner W 2001 *Phys. Rev. E* **64** 016414
[9] Santala M I K *et al* 2001 *Appl. Phys. Lett.* **78** 19
[10] Pretzler G *et al* 1998 *Phys. Rev. E* **58** 1165
[11] Habara H *et al* 2004 *Phys. Rev. E* **70** 046414
[12] Belyaev V S, Vinogradov V I, Matafonov A P, Krainov V P, Lisitsa V S, Andrianov V P and Ignatyev G N 2006 *Laser Phys.* **16** 1647
[13] Key H M *et al* 1998 *Phys. Plasmas* **5** 1966
[14] Yang J M *et al* 2004 *J. Appl. Phys.* **96** 6912
[15] Habara H, Kodama R, Sentoku Y, Izumi N, Kitagawa Y, Tanaka K A, Mima K and Yamanaka T 2004 *Phys. Rev. E* **69** 036407
[16] Izumi N *et al* 2002 *Phys. Rev. E* **65** 036413
[17] Toupin C, Lefebvre E and Bonnaud G 2001 *Phys. Plasmas* **8** 1011
[18] Shen B, Zhang X and Yu M Y 2005 *Phys. Rev. E* **71** 015401(R)
[19] Macchi A 2006 *Appl. Phys. B* **82** 337
[20] Macchi A, Cattani F, Liseykina T V and Cornolti F 2006 *Superstrong Fields in Plasmas: 3rd Int. Conf. of Superstrong Field in Plasma* (*Varenna, Italy, 19–24 September 2005*) ed D Batani and M Lontano (New York: AIP) p 215
[21] Sentoku Y, Kemp A J, Presura R, Bakeman M S and Cowan T E 2007 *Phys. Plasmas* **14** 122701
[22] Miyamoto S, Kato S, Takamaru H, Horiuchi R and Sato T 1997 *J. Plasma Fusion Res.* **73** 343
[23] Petrov G M and Davis J L 2008 *Plasma Phys. Control. Fusion* **50** 015004
[24] Jackson J D 1975 *Classical Electrodynamics* (New York: Willey) p 647
[25] Dupree S A and Fraley S K 2002 *A Monte Carlo Primer: A Practical Approach to Radiation Transport* (New York: Kluwer/Plenum) p 89
[26] Marion J B and Fowler J L 1960 *Fast Neutron Physics* (New York: Interscience) p 73
[27] Halpern G M and Kim H-G 1978 *J. Appl. Phys.* **49** 3784
     Fritz J N 1999 *Shock Compression of Condensed Matter* ed M D Furnish *et al* (New York: AIP) p 145
[28] Bichsel H and Inokuti M 1998 *Nuclear Instrum. Methods Phys. Res. B* **134** 161
[29] Astner G, Mannervik S and Veje E 1981 *Nuclear Instrum. Methods* **188** 475
[30] Pukhov A 2001 *Phys. Rev. Lett.* **86** 3562
[31] Sentoku Y, Mima K, Sheng Z M, Kaw P, Nishihara K and Nishikawa K 2002 *Phys. Rev. E* **65** 046408
[32] Sentoku Y, Mima K, Ruhl H, Toyama Y, Kodama R and Cowan T E 2004 *Phys. Plasmas* **11** 3083
[33] Ledingham K W D, McKenna P and Singhal R P 2003 *Science* **300** 1107
[34] Santry D C and Werner R D 1981 *Nuclear Instrum. Methods* **188** 211